2022

# Theoretical investigation of SOFC/SOEC degradation mechanisms and mitigations

Fuming Jiang
*West Virginia University*, jifuming@mix.wvu.edu

# Theoretical investigation of SOFC/SOEC degradation mechanisms and mitigations

Fuming Jiang

Problem Report submitted to the Benjamin M. Statler College of Engineering and Mineral Resources at West Virginia University

in partial fulfillment of the requirements for the degree of

Materials Science and Engineering in
Mechanical and aerospace engineering

Yun Chen, Ph.D., Chair
Xueyan Song, Ph.D.
Ever J. Barbero, Ph.D.

Department of mechanical and aerospace engineering

Morgantown, West Virginia
July 2022

Keywords: Degradation, SOEC, SOFC, delamination, Cr poisoning, Oxygen partial pressure, Interface, TPB

ABSTRACT

Theoretical investigation of SOFC/SOEC degradation mechanisms and mitigations

Fuming Jiang

America has a rapid growth in the development of renewable power generation in the twenty-first century. Hydrogen energy especially is the major topic in development of renewable power generation because it has the ability to provide for energy in transportation, combined heat and power generation and energy storage systems with little or no impact on the global ecosystem. Electrolysis and fuel cell technology for hydrogen energy storage has brought interest to the researchers worldwide.

Solid oxide electrolysis cells (SOECs) and Solid oxide fuel cells (SOFCs) are promising hydrogen energy technologies that can utilize chemical energy to produce and store electricity. SOEC can produce hydrogen at a higher chemical reaction rate with a lower electrical energy requirement. SOFCs offer significant advantages in the variety of fuels, quiet operation, low or zero emission and high efficiency.

The performance of SOECs and SOFCs is the key for commercializing SOECs and SOFCs. This work presents the methods and theory of improving the performance of SOECs and SOFCs. A thermodynamic and electrochemical equilibrium model is established for SOECs by considering a cathode/electrolyte interfacial porous layer. By using numerical experiments, the one dimensional thermodynamic and electrochemical equilibrium model with porous layer provides a guideline for designing and optimizing SOECs. The mechanisms of SOFCs degradation are reported and the ideal maximum oxygen partial pressure is calculated to avoid SOFCs degradation

**Table of Contents**

## List of Figures

# 1. Introduction

## 1.1 Main components and working principle of SOEC/SOFC cell

- **Solid oxide fuel/electrolysis cell (SOEC/SOFC) as a new large-scale energy storage technique**

The energy crisis and the high demand of fossil fuel lead the gas price in the U.S. to a new level. The International Energy Agency reported the U.S. industrial sector's energy consumption will grow more than twice as fast as any other end-use sector from 2021 to 2050. The states need renewable energy to replace fossil fuels. Under the situation of exhausting fossil energy and worsening environment, electrolysis technology for hydrogen energy storage has been a subject of intense interests worldwide [1]. Hydrogen energy storage is considered to be of extremely potential for new large-scale energy storage technique in the future due to its advantages such as sustainable, environment friendly, long lifetime and cost effective.

The water electrolysis technology is the key point in the hydrogen energy storage system, currently three kinds of electrolysis configurations are developed based on different electrolytes; Alkaline electrolysis cell (AEC), solid polymer electrolyser (SPE) and solid oxide electrolysis cell (SOEC), respectively. A solid oxide fuel cell (SOFC) that runs in regenerative mode to achieve the electrolysis of water and which uses a solid oxide, or ceramic, electrolyte to produce oxygen and hydrogen gas. SOEC shows great merits in contrast to the AEC and SPE, e.g., the efficiency of hydrogen production for high temperature SOEC is more than twice of that for AEC, and is 1.5 times of that of proton exchange membrane electrolyser [2]. Therefore high temperature water electrolysis using SOEC is so far the most promising method for generating hydrogen efficiently. It makes energy use efficient and clean.

SOFC is one of the promising renewable energy technologies can utilize chemical energy to produce electricity [3,4]. Additionally, high-temperature (800-1000 ˚C) SOFC has a high-temperature exhaust streams thus the exhausts can be utilized again with gas turbine, steam turbine to achieve high-efficiency combined cycle combinations according to DED [5]. As electricity power become more and more easy and effectively to collect, such as solar energy, wind turbines, hydroelectric plants, nuclear power plants etc., there is large excessive power being wasted during low electricity consumption period. SOFC and SOEC are excellent devices that can store energy and generated energy as needed.

- **Main components and working principle of SOFC/SOEC cell**

SOFC consists of a solid electrolyte, an anode and a cathode as shown in Fig. 1.1 [6]. In the fuel cell, diffusion of oxygen molecules takes place at cathode and becomes oxygen ions which in turn pass through electrolyte and reacts with gaseous fuel at node thus producing electricity [7]. Hydrogen fuel is fed into the anode of the fuel cell and oxygen from the air, enters the cell through the cathode. By burning fuel containing hydrogen on one side of the electrolyte, the concentration of oxygen is greatly reduced. The electrode on this surface will allow oxygen ions to leave the electrolyte and react with the fuel, which is

oxidized, thereby releasing electrons ($e^-$). On the other side of the plate, which is exposed to air, an oxygen concentration gradient is created across the electrolyte, which attracts oxygen ions from the air side, or cathode, to the fuel side, or anode. If there is an electrical connection between the electrodes, electrons flow from anode to cathode where a continuous supply of oxygen ions ($O^{2-}$) for the electrolyte is maintained and oxygen ions from cathode to anode, maintaining overall neutral charge thus generating useful electrical power from the combustion of the fuel. The only byproduct of this process is a pure water molecule ($H_2O$) and heat [8].

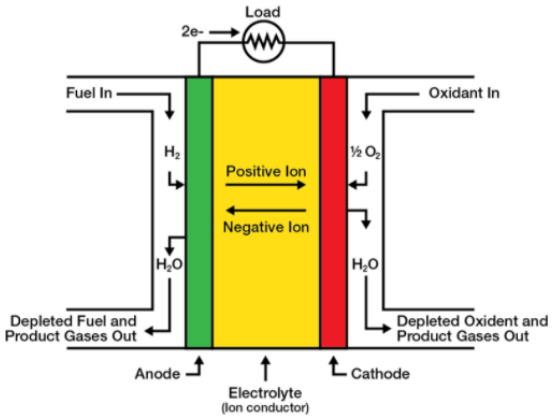


Figure 1.1 Schematic of SOFC [6]

The reactions taking place at anode and cathode are given as follows:
Reactions at anode:

$$H_2 + O^{2-} \rightarrow H_2 + 2e^- \quad (1\text{-}1)$$

$$CO + O^{2-} \rightarrow CO_2 + 2e^- \quad (1\text{-}2)$$

$$CH_4 + O^{2-} \rightarrow 2H_2O + CO_2 + 8e^- \quad (1\text{-}3)$$

Reactions at cathode:

$$O^2 + 4e^- \rightarrow 2O^{2-} \quad (1\text{-}4)$$

The reactions on the SOFC makes SOFCs are ideal for carbon capture in that the fuel and oxidant (air) streams can be kept separate by design, thereby facilitating high levels of carbon capture without substantial additional cost [7].

SOEC uses electricity to split water molecules ($H_2O$), carbon oxides, sulphur oxides and nitrogen oxides into hydrogen ($H_2$) or other fuels and oxygen ($O_2$).

Take water as an example, water molecules diffuse to the reaction sites and are dissociated to form hydrogen gas and oxygen ions at the cathode–electrolyte interface. The hydrogen gas diffuses to the cathode surface and gets collected. The oxygen ions are transported through the dense electrolyte to the anode. the oxygen ions are oxidized to oxygen gas and the produced oxygen is transported through to the anode surface. SOEC also consists of a solid electrolyte, an anode, and a cathode however, the anode and cathode are reversed as from SOFC. The working environment and electrode reaction

process of SOEC are quite different from those of SOFC, bringing many challenges for the selection of electrode materials. The reactions taking place at anode and cathode are shown in Fig. 1.2 [9].

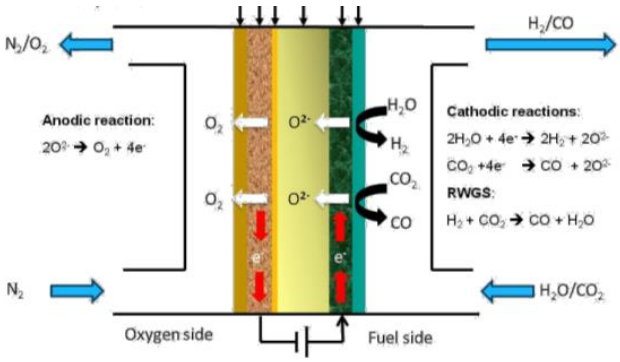


Figure 1.2 Schematic of SOEC [9]

## 1.2 Background of the state of art SOFC/SOEC progress

- **State-of-the-art hydrogen fuel cells**

Artificial Intelligent (AI) assisted SOFC system

AI has been applied to SOFC system recently, a locating method combining long short-term memory artificial neural network (LSTM) and causal inference is used. The literature reported that they can locate different faults with an accuracy of 92.6% [10]. AI has also used to provide more reliable and more accurate results for determine performance parameters of the commercialized SOFC stacks before construction [11]. In order to achieve the proper performance parameters, a modified metaheuristic algorithm, called the Fractional Order Dragonfly algorithm is utilized. This algorithm was utilized for the sum of squared error (SSE) minimization between the outputted voltage of the empirical data and the obtained data.

Oxygen-conducting electrolytes

Complex oxides based on $LaGaO_3$ offer a convenient basis for the design of oxygen-conducting electrolytes for solid oxide fuel cells [12]. A rational combination of appropriate dopants incorporated at various sublattices of LaGaO3 allows superior transport properties to be achieved for co-doped derivatives ($La_{1-x}Sr_xGa_{1-y}Mg_yO_{3-\delta}$, LSGM). It was shown in [13] that the ion-transfer numbers were nearly equal to 1. For $La_{0.9}Sr_{0.1}Ga_{0.8}Mg_{0.2}O_{3-\delta}$ and $La_{0.8}Sr_{0.2}Ga_{0.8}Mg_{0.2}O_{3-\delta}$ ceramic samples, the oxygen-ion transference numbers were found to be equal 1 at 700–1000 °C [14], confirming the presence of electrolyte-type behavior.

The most investigated and state-of-art SOEC is composed of a nickel and yttria stabilized zirconia (YSZ) composite (Ni-YSZ) cathode, YSZ oxygen-ion conducting electrolyte, as well as lanthanum strontium manganite and YSZ (LSM-YSZ) anode. Excessive amount of oxygen is generated as the result of the distribution of vacancies in the YSZ/LSM interface, and it leads to peeling of oxygen electrode and increase of polarization resistance [15,16,17]. Pattaraporn [18] compared the electrolysis performance of SOEC using LSM-YSZ as well as $(La,Sr)(Co,Fe)O_3$ (LSCF) as oxygen electrode at 550-800 ˚C. The result

indicated that LSCF shows greater electrochemical activity than LSM, mainly because LSCF features both ionically and electrically conducting, as well as lower polarization resistance [19].

- **State-of-the-art hydrogen electrolysis cell**

New materials and micro-structure design is proposed for improving the SOECs' performance. Ni–Fe alloy nanoparticles embedded in ceramic $Sr_2Fe_{1.5}Mo_{0.5}O_{6-\delta}$ (SFM) achieved direct $CO_2$ electrolysis with a current density of 2.66 A $cm^{-2}$ [20] A Novel Micro-/Nano Channel Anode design as shown in the figure 1.3 achieved a current density of 5.96 A $cm^{-2}$ at 800 °C [21].

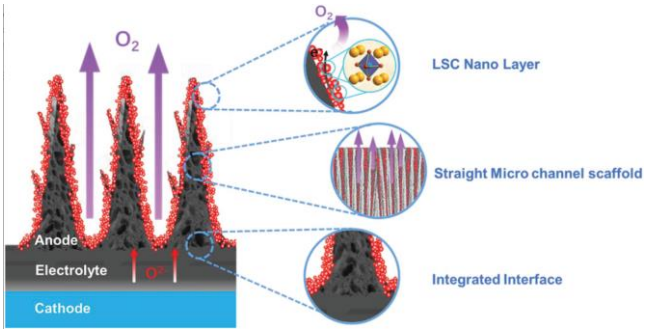


Figure 1.3 the Micro-/Nano Channel Anode design [21]

The current density of the reviewed SOECs is very promising, however they both have short life-time. In the SFM ceramic electrode SOEC experiment, the researchers only performed a stability test of 140 hours. For the Novel Micro-/Nano Channel Anode design experiment, the current density of 5.96 A $cm^{-2}$ is achieved for about 200 minutes.

Most oxygen electrodes consist of mixed conducting perovskite type oxides with $ABO_{3-\delta}$. as general composition. This report listed 3 different materials for the oxygen electrodes of SOECs.

$La_{0.8}Sr_{0.2}MnO_{3+d}$ (LSM) is the oldest oxygen electrode material commercially used for high-temperature SOEC, typically 800-900 °C [22]. $La_{0.6}Sr_{0.4}Co_{0.2}Fe_{0.8}O_{3-d}$ (LSCF) has excellent mixed ionic and electronic conductivity, it is usually used in the intermediate-temperature [23]. $Ba_{0.5}Sr_{0.5}Co_{0.8}Fe_{0.2}O_{3-\delta}$ (BSCF), BSCF has fast bulk oxygen transportation, the reported highest oxygen ionic conductivities is 0.07 Siemens /cm at 600 °C and 0.24 S/cm at 700 °C, it stands out because of its ultrahigh ionic conductivity and excellent electrocatalytic activity, but it is still very subject to instability [24]. To this date, LSCF and LSM are still the most popular selections for the SOECs electrodes materials.

- **Future improvement for state-of-the-art SOFC/SOEC**

For large-scale commercialization of SOFC in applications ranging from distributed-generation to utility-scale power applications, a long-term durability

of SOFCs is at least 40,000 hours, with a maximum degradation rate of 0.2% per 1000 hours [25].

For Stable SOECs, it is reported that with high current density of 3 A/cm$^2$ for 1000 hours operation is achievable [26]. However, the reported results are questionable, up to date, it is still very hard to replicate the same performance for the researchers.

The long-term durability of SOFCs/SOECs are still a major factor for them to be fully commercialized.

## 1.3 Overview of SOEC degradation phenomena and hypothesis of the mechanisms: electrode/electrolyte interface

- **Phenomena of SOEC anode delamination from the electrolyte**

The high temperature and severe electrochemical conditions in a solid oxide cell require development and improvement of promising materials and create important challenges to the longevity and durability of the different cell components. Therefore, it is important to understand and address the reasons of degradation in SOECs. In the SOEC degradation, delamination is the major issues need to be improved. The most common mode of failure has been reported to the occurrence of delamination at the oxygen electrode/electrolyte interface. Thus, the investigations of the delamination are mainly focused on the oxygen electrode/electrolyte (YSZ) interface.

SOEC components [2,15-17], as the origin of SOEC degradation is often difficult to determine. SOEC anode delamination from the electrolyte is a major known contribution to performance degradation. The cathode suffers irreversible degradation under high steam concentration which causes agglomeration of nickel and leads to the formation of nickel hydroxide and also low hydrogen partial pressures. The 8YSZ (8 mol% $Y_2O_3$ stabilized $ZrO_2$) solid electrolyte shows pore formation at the interface with anode. $SrZrO_3$ formation is observed in pores of the cerium gadolinium oxide (CGO) diffusion barrier layer [18]. The oxygen electrode material has a dominant role in the degradation of the SOEC [19,27,28].

Long-term SOEC operation of the cells is reported in Refs. [1,2]. Degradation rates are given in Refs. [1,2,15]. Because the electrochemical performance is described in detail elsewhere [18], the literature concentrates on additional investigations on degradation phenomena in the previously described SOEC tests. Researchers investigated on the aging processes using X-ray diffraction (XRD), scanning electron microscopy (SEM), transmission electron microscopy (TEM) and Mössbauer spectroscopy. The structural and morphological changes of the oxygen electrode during operation the SOEC are reported.

In SOEC, Fig. 1.4 shows an SEM micrograph of a delaminated oxygen electrode [29,30,31]. The delamination is reported in the long-term cell life tests [32] as shown in Fig. 1.4. The cell tested as SOFC shows an overall voltage degradation of 0.8%/1000 h, while a higher degradation rate of 8.3%/1000 h was observed for the cell tested as SOEC. The comparison results show that SOEC exhibits about 10 times larger attenuation than SOFC.

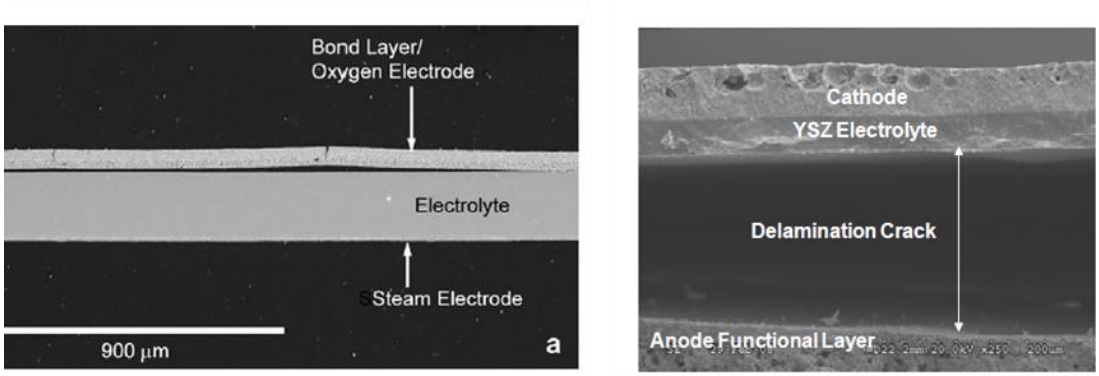


Figure 1.4 SEM micrographs from Mawdsley et al [30] and Virkar et al [31] showing oxygen electrode delamination along the oxygen electrode/electrolyte interface.

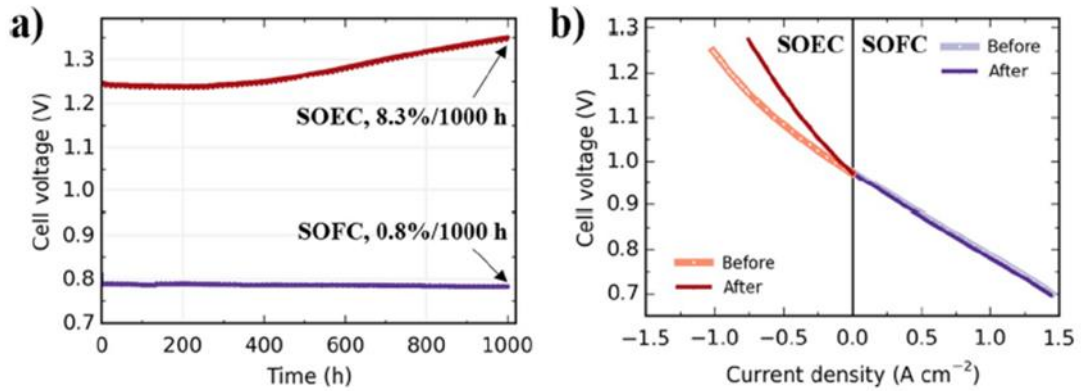


Figure 1.5 Comparison of electrochemical durability for SOFC and SOEC operation. a) Voltage profile as a function of time. b) I–V curves recorded before and after the durability tests [32].

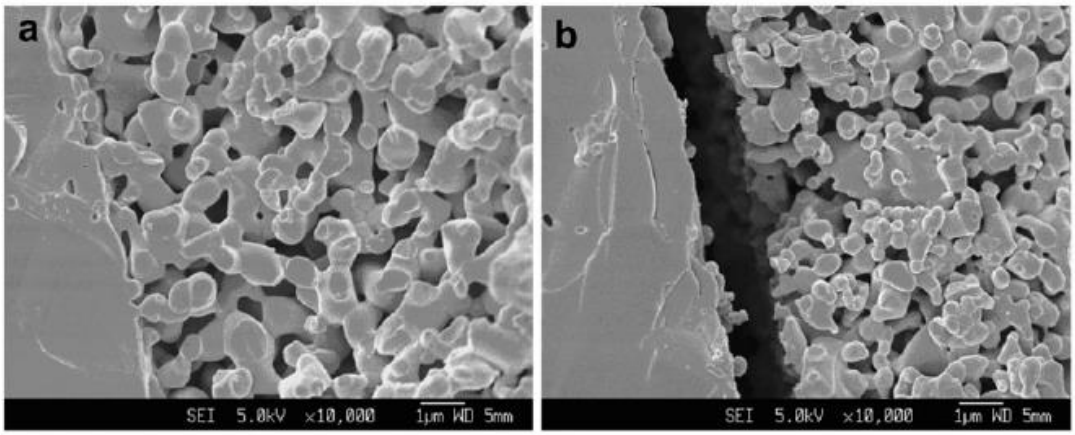


Figure 1.6 SEM micrographs of the cross-section of LSM oxygen electrode/YSZ electrolyte interface (a) before and (b) after anodic polarization at 500 mA cm$^{-2}$ and 800 ˚C for 48 h [16]

After polarized at 500 mA cm$^{-2}$ for 48 h, there are decrease in LSM grain size and clearly a gap formed between the LSM oxygen electrode and YSZ

electrolyte (Fig. 1.6b), indicating the delamination and failure of the LSM oxygen electrode.

There are 3 different hypotheses of the mechanisms to explain the delamination and failure of the LSM oxygen electrode.

### 1.2.1 Delamination caused by high oxygen partial pressure

One of the obvious phenomena is the high oxygen partial pressures at the electrode/electrolyte interface, the delamination had happened when oxygen pressure reached $2.3\times10^4$ atm. In fact, a typical temperature of electrolysis of 800 ˚C, for values of (corresponding to $p_{O_2}^{a}$=100 atm) delamination may occur along the oxygen electrode/electrolyte interface [29, 31,33]. The high pressure formed just inside the electrolyte links up with the near surface defects causing delamination. An important consequence of non-equilibrium thermodynamics is the occurrence of abrupt changes in 'potentials' (chemical and/or electrical) across interfaces [33].

Despite the wide-ranging observations on cation segregation on perovskite-type oxides, the answer to how such surface segregation layers influence the oxygen reduction and evolution kinetics remains controversial. Rational design of novel materials and structures to improve the activity and durability of solid oxide cell materials also requires the advancement of our knowledge on the electrochemical reaction and degradation mechanisms at the molecular level [34]. More understanding on the electrochemical reaction and degradation mechanisms is needed.

- **Porous layer at the electrolyte/anode interface to prevent the delamination**

By considering the diffusion path of the oxygen ion at the electrolyte/anode interface, YSZ porous layer was prepared on both sides of YSZ electrolyte to prevent the delamination of the interface.

YSZ porous layer was prepared on both sides of YSZ electrolyte by spin-coating. The sample with YSZ porous layer between dense electrolyte and LSM electrode was named to W-PL, and the sample without YSZ porous layer was named to N-PL as shown in Fig. 1. 7.

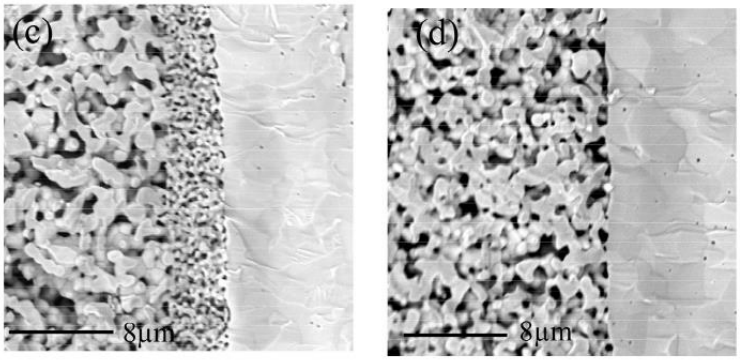


Figure 1.7 The cross sectional of (c)W-PL, (d)N-PL [35].

Under anodic polarization, oxygen ion transports though the YSZ electrolyte via bulk and grain boundaries. The oxygen gas at the closed pores/cavities could diffuse into the air by redox reaction due to oxygen activity difference. The diffusion path of the oxygen ion at closed pores of W-PL is shorter than that of N-PL due to the difference of YSZ particle size. Therefore, the oxygen gas at closed pores/cavities at the solid-solid two-phase (oxygen electrode and electrolyte) interface for W-PL could diffuse rapidly into air. But the oxygen gas oxidized at the YSZ grain boundaries are accumulated at the closed pores/cavities of electrolyte of N-PL, resulting in the high oxygen pressure/activity at the electrode/electrolyte interface [36]. The experiments cannot fully explain the electrochemical mechanism for the addition of porous layer. Thus, a model of the porous layer for electrochemical mechanism needs to be considered.

The oxygen pressure at the solid-solid two-phase (oxygen electrode and electrolyte) interface (SSTPI) could be calculated according to the Nernst equation:

$$E_N = \frac{RT}{4F} \ln \left( \frac{p_{O_2}^{O_x}}{p_{O_2}^{St-H_2}} \right) \quad (1\text{-}5)$$

where $p_{O_2}^{O_x}$ and $p_{O_2}^{St-H_2}$ are the oxygen pressure at the SSTPI and the reference electrode, respectively. The reference electrode of W-PL and N-PL are directly exposed to air, so $p_{O_2}^{St-H_2}$ is the same.

Thus, the oxygen pressure at the SSTPI of samples were calculated. the oxygen pressure at the SSTPI of N-PL was 0.41 atm, still larger than oxygen partial pressure in air, meaning that certain amount of oxygen gas accumulates at closed pores/cavities of electrolyte. While, the oxygen pressure at the SSTPI of W-PL had reached 0.21 atm rapidly, indicates that oxygen gas accumulates at closed pores/cavities of electrolyte diffuses rapidly toward the air.

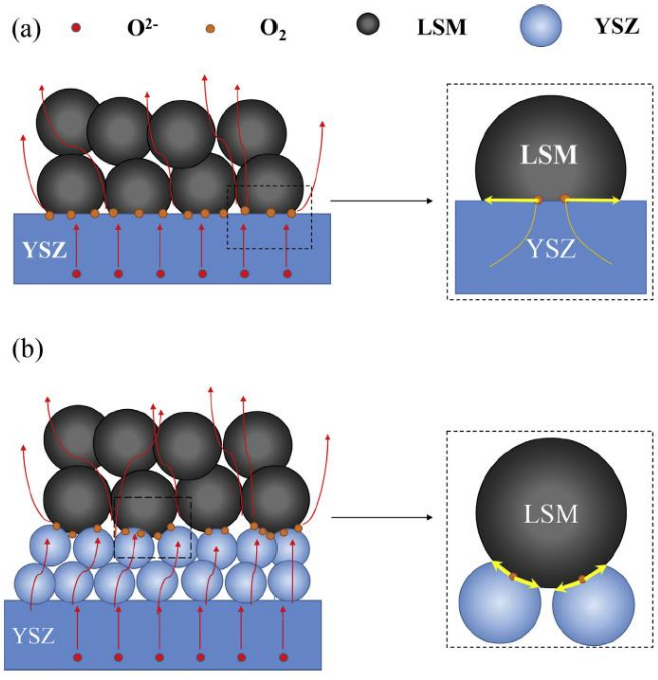


Figure 1.8 The schematic diagram of the oxygen oxidation reaction at the SSTPI for (a) N-PL, (b) W-PL [35]

Figure 1.8 shows the schematic diagram of the oxygen oxidation reaction for (a) N-PL, (b) W-PL. Under anodic polarization, oxygen ion transport though the YSZ electrolyte via bulk and grain boundaries, are oxidized to oxygen gas at the three phase boundary (TPB) and SSTPI, respectively. The oxygen gas oxidized at the YSZ grain boundaries are accumulated at the closed pores/cavities of electrolyte, resulting in the high oxygen pressure/activity at the SSTPI.

The oxygen gas at the closed pores/cavities could diffuse into the air by redox reaction due to oxygen activity difference. The diffusion path (yellow line) of the oxygen ion at closed pores of W-PL is shorter than that of N-PL due to the difference of YSZ particle size. Therefore, the oxygen gas at closed pores/cavities at the SSTPI for W-PL could diffuse rapidly into air.

In results the introduced YSZ porous layer on dense electrolyte not only extends oxygen oxidation reaction sites, but also provides shorter path for oxygen ion diffusion at the SSTPI to enhance performance and stability of LSM electrode.

- **Local Ni depletion as a major source of the SOEC performance degradation**

For what concerns SOEC operation, some degradation phenomena responsible for the microstructural degradation of the fuel electrodes have been identified: carbon deposition, impurity segregation, percolation loss due to formation of $ZrO_2$ nanoparticles, Ni coarsening and Ni depletion. More recently The et al. observed Ni coarsening and Ni depletion in the innermost region of the active fuel electrode for SOECs tested at 0.75 A $cm^{-2}$ (6100 h) and 1 A $cm^{-2}$ (9000 h) [37].

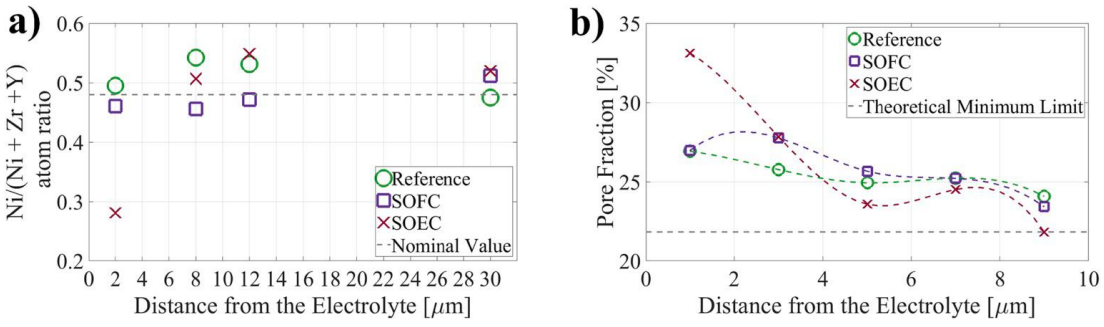


Figure 1.9. EDS results a) and porosity quantification performed on SEM images b) for the three samples analyzed. the nominal value for the Ni ratio in Figure 1.9 a (0.48) is calculated based on cell manufacturing data. The theoretical minimum limit for the pore fraction shown in Figure 1.9 b (21.8%) is calculated based on porosity only originating from the reduction of NiO to Ni for a Ni/YSZ electrode with a Ni/YSZ volume ratio of 40/60 [32].

Figure. 1.9 a shows a significant Ni depletion in the SOEC at a distance of 2 μm from the electrode/electrolyte interface, the ratio (Ni/(Ni + Zr + Y)) decreases from ~0.49 for the reference sample to ~ 0.28 for the cell aged in SOEC mode. This loss of Ni in the region close to the SOEC electrode/electrolyte interface reduces the electronic conductivity and the number of active sites for electrochemical reaction, as confirmed by FIB-SEM results, which show the decrease of both total and percolating TPB density. The more pronounced decrease of TPB observed for the SOEC indicates that Ni depletion plays the primary role to the increase of the overpotential.

Mogens et al. proposed that the driving force for the Ni migration is the formation of $Ni(OH)_x$ volatile species which diffuse down the steam partial pressure gradients [38].

It has been reported that the contact angle is a function of the oxygen partial pressure ($p_{O_2}$) [39].

$$p_{O_2} = \frac{1}{K_H}\left(\frac{p_{H_2O}}{1 - p_{H_2O}/P_{tot}}\right) \quad (1\text{-}6)$$

where $K_H$ is the equilibrium constant for the $H_2/O_2$ reaction and equal to 2.33 x $10^{18}$ at 800 ˚C.

Ni migration in the SOEC leads to loss of percolating nickel and an increase in the porosity in the active region of the fuel electrode. Furthermore, the more pronounced decrease of the SOEC total and percolating TPB density will affect the electrical performance of the cell. From the results we emphasize that local Ni depletion should be considered a major source of the SOEC performance degradation. The Ni moves from the position of very low $p_{O_2}$ (strongly polarized zone close to the electrolyte) where the Ni/YSZ contact angle is high (de-wetting) towards the higher $p_{O_2}$ in the outer parts of the electrode, that are less polarized and where also the gas phase $p_{O_2}$ is higher, resulting in a locally lower Ni/YSZ contact angle (wetting behavior).

### 1.2.2 Delamination caused by lattice shrinkage and coarsening

- **Hypothesis of the mechanisms of lattice shrinkage**

The decrease in LSM grain size is due to the shrinkage of the LSM lattice, which is explained by the incorporation of excess oxygen under oxidation conditions and consequent valence increase of Mn ions at the LSM B-site and/or the increase of the cation vacancies [40]. Such shrinkage of the LSM lattice also reported in [41].

Partial doping of the $La^{3+}$ site in $LaMnO_3$ perovskites with low-valence cations (e.g., $Sr^{2+}$) will lead to an increase in the valence of the B-site Mn metal ions (as positive holes) and/or the formation of oxygen vacancies. According to the

defect model two defect equilibria can be written as a function of partial pressure of oxygen and temperature:

$$O_{O,LSM}^{X} + 2Mn_{Mn}^{\cdot} \leftrightarrow V_{\ddot{O},LSM} + 2Mn_{Mn}^{\times} + \frac{1}{2}O_2 \quad (1\text{-}7)$$

$$O_{O,LSM}^{X} + 2Mn_{Mn}^{\times} \leftrightarrow V_{\ddot{O},LSM} + 2Mn_{Mn}^{'} + \frac{1}{2}O_2 \quad (1\text{-}8)$$

where $Mn_{Mn}^{\cdot}$, $Mn_{Mn}^{\times}$, and $Mn_{Mn}^{'}$ donate $Mn^{4+}$, $Mn^{3+}$, and $Mn^{2+}$ ions, respectively, and $O_{O,LSM}^{X}$ and $V_{\ddot{O},LSM}$ stand for $O^{2-}$ ions and oxygen vacancies in LSM lattice sites.

Once the oxidation state of Mn ions reaches 4+, the excess oxygen migrated or incorporated at the LSM electrode lattice would be compensated by the formation of Mn cation vacancies. The formation of cation vacancies would cause the lattice shrinkage.

The formation of nanoparticles within LSM particles is most likely due to the migration or incorporation of oxygen ions from the YSZ electrolyte into LSM grain bulk, resulting in the LSM lattice shrinkage due to the oxidation of manganese ions and formation of manganese cation vacancies. The lattice shrinkage would lead to the local tensile strains within the LSM particles and subsequent formation of microcracks and nanoparticles at the interface.

- **Cause of delamination**

In the case of conventional LSM–YSZ oxygen electrodes, excess lattice shrinkage within LSM grains at the interface can cause the buildup of internal stress, leading to the formation of LSM nanoparticles and the delamination of LSM electrodes. Fig. 1.10. shows schematically the delamination process of an LSM oxygen electrode un0der SOEC operation conditions.

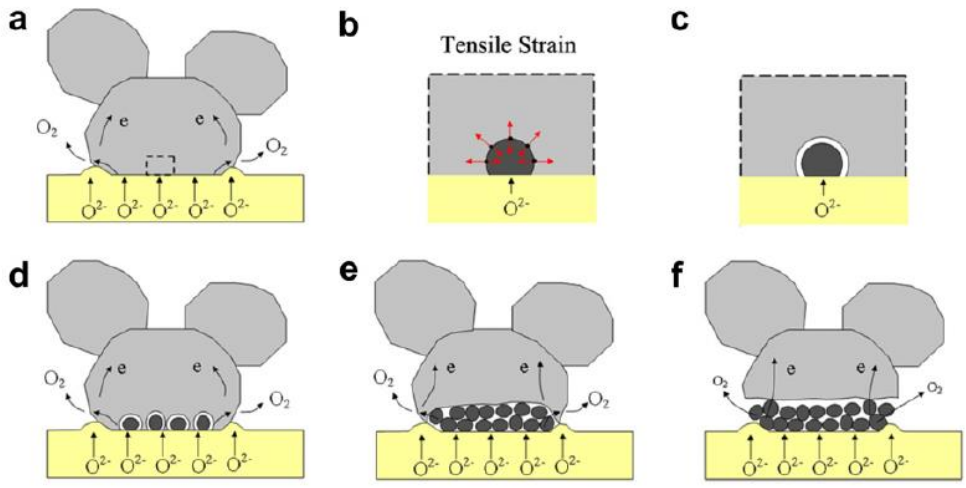

Figure 1.10 Schematic illustrations of the microstructural change of the LSM oxygen electrode/YSZ electrolyte interface under SOEC operation conditions: (a) oxygen migration from YSZ electrolyte to LSM grain bulk at the interface, (b) local tensile strains within LSM particles due to the shrinkage of LSM lattice, (c) local tensile strains induced microcrack formation, (d) formation of individual nanoparticles, (e) propagation and continuous nanoparticles formation and LSM grain is bonded to YSZ electrolyte through bridges along edge of the convex contact ring, and (f) formation of complete nanoparticle layers and delamination of the LSM oxygen electrode under high internal oxygen partial pressure at the interface [16].

The migration of oxygen ions from YSZ electrolyte to the LSM particles at the electrode/electrolyte interface would result in the localized internal stress in the LSM region next to the YSZ interface due to the lattice shrinkage as described above (Fig. 1.10 b).

It can also be considered that such microcrack formation can only occur within LSM particles bonded to YSZ electrolyte. For the LSM particles not in contact with the YSZ electrolyte, the incorporation of oxygen ions would only result in a globe LSM lattice shrinkage but not local tensile-strains due to the free-standing of LSM grains in the bulk of the electrodes.

- **Different stability behavior of lattice shrinkage and coarsening [42]**

From the results of other studies [40] under polarization condition, both lattice shrinkage and lattice expansion could happen. As shown in Fig. 1.11, in the case of electrodes heat-treated at 900 °C with the initial average nanoparticle size of 66±18 nm, the grain growth kinetics by the thermal coarsening effect is dominant, indicated by the increase of LSM nanoparticles after anodic polarization test, while for the electrode heat-treated at 1100 °C with the initial average nanoparticle size of 157±34 nm, the lattice shrinkage effect plays a dominant role in controlling the microstructural behavior of the infiltrated LSM nanoparticles, supported by the decrease of the LSM particle size polarized under identical conditions. The study demonstrates that the long-term stability of nano-structured LSM–YSZ composite oxygen electrodes could be manipulated by controlling and optimizing of the infiltrated LSM nanoparticles. The LSM lattice shrinkage effect under anodic electrolysis polarization is the main reason for the observed excellent stability of the infiltrated LSM–YSZ composite oxygen electrodes. In the case of nanostructured LSM–YSZ oxygen electrodes, the microstructural stability of LSM nanoparticles is governed by two opposite effects; one is the grain growth by the thermal sintering effect and the other is the LSM lattice shrinkage under the anodic polarization. The process that is dominant for the microstructural behavior of infiltrated LSM nanoparticles appears to be related to the initial particle size of the infiltrated LSM [42].

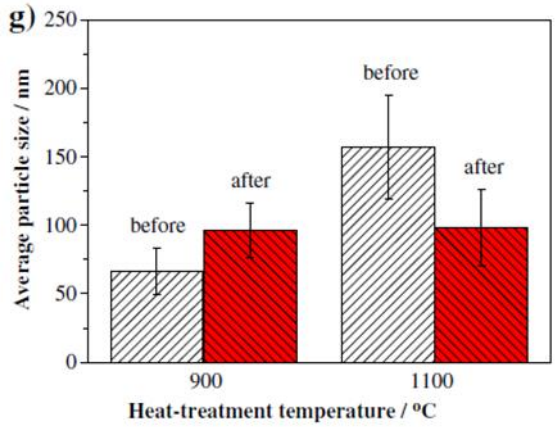


Figure 1.11 The average particle size of infiltrated LSM nanoparticles before and after polarization is shown in (g) [42].

The SEM micrographs of the YSZ scaffold and the infiltrated LSM–YSZ electrodes before and after the polarization stability test are shown in Fig. 1.12. For the electrode heat-treated at 900 °C with the initial average nanoparticle size of 66±18 nm, the grain growth kinetics by the thermal coarsening effect is dominant, indicated by the increase of LSM nanoparticles after anodic polarization test. As shown in Fig. 1.12c and Fig. 1.12e. For the electrode heat-treated at 1100 °C with the initial average nanoparticle size of 157±34 nm, the lattice shrinkage effect plays a dominant role in controlling the microstructural behavior of the infiltrated LSM nanoparticles, supported by the decrease of the LSM particle size polarized under identical conditions. As shown in Fig. 1.12d and Fig. 1.12f.

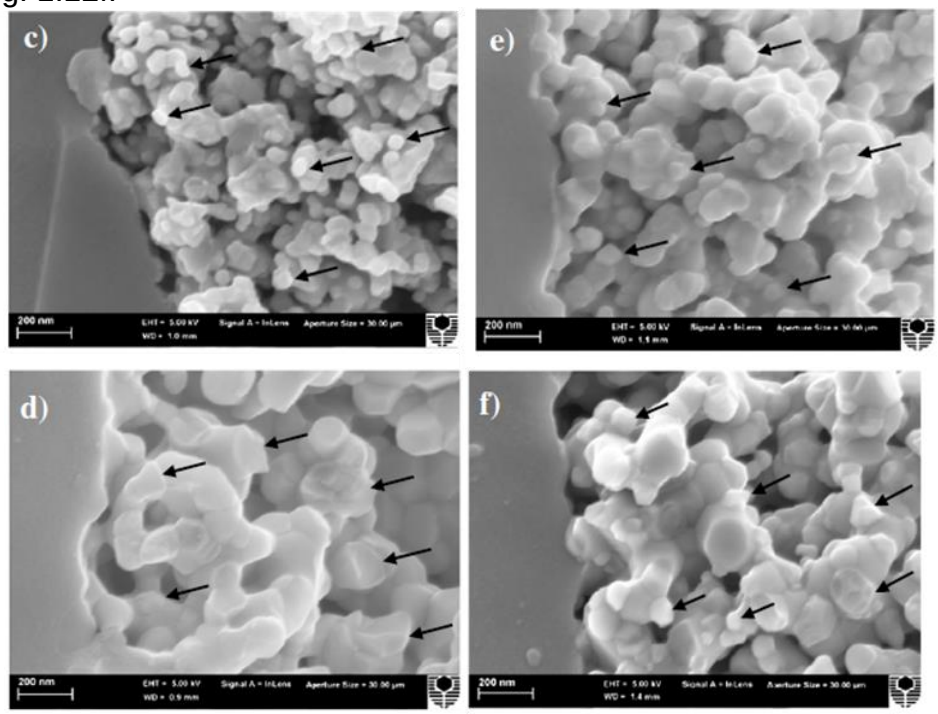


Figure 1.12 SEM micrographs of the cross sections of freshly infiltrated LSM–YSZ electrodes heat-treated at (c) 900 °C and (e) after polarization at 500 mA $cm^{-2}$ at 800 °C for 100 h, heat-treated at (d) 1100 °C and (f) after polarization at 500 mA $cm^{-2}$ at 800 °C for 100 h [42].

For the electrode heat-treated at 900 °C (Fig. 1.13a), there is small increase in $\eta_{anodic}$ and $R_E$ in the early stage of polarization for 30 h, followed by a relatively stable performance with further polarization. $R_E$ is very stable while the electrode ohmic resistance, $R_\Omega$ appears to show a very small increase with the polarization. For the electrode heat-treated at 1100 °C, $R_E$ decreased from the peak value of 0.93 to 0.62 Ω cm$^2$ after being polarized for 100 h (Fig. 1.13b), showing the enhancement of the performance stability of the electrode. The $R_\Omega$ is more or less stable except for a very small increase at the early stage of polarization.

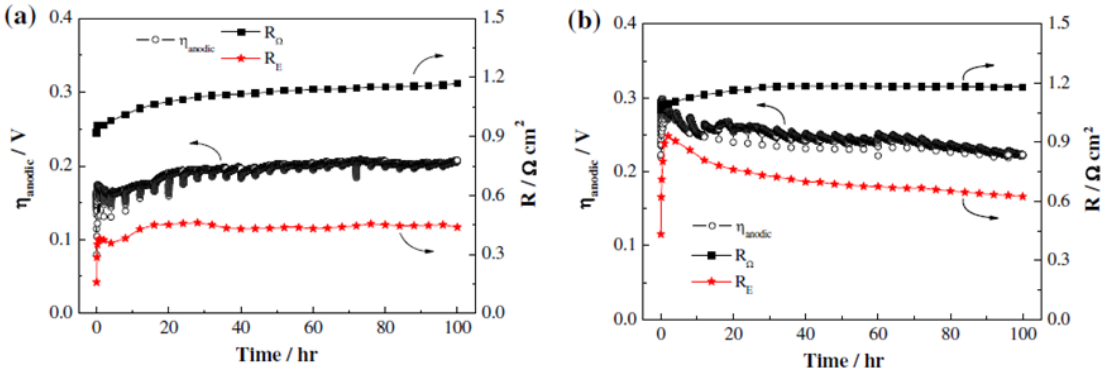


Figure 1.13 Polarization curves for the infiltrated LSM–YSZ electrodes heat-treated at (a) 900 and (b) 1100 °C, measured at 500 mA cm$^{-2}$ and 800 °C for 100 h [42].

### 1.2.3 Atomic-scale mechanisms of oxygen electrode delamination

Many of degradation processes in materials start with individual atomic-scale defects that form, interact with each other, transform into another types of defects, and cause instabilities and imperfections at larger length scales.

Atomic-scale models for YSZ surface and LSM/YSZ interface are shown in Fig.1.14. Fig. 1.14b shows relaxed structure of the $LaMnO_3/ZrO_2$ interface obtained by positioning a (001) surface of $LaMnO_3$ on top of oxygen saturated (001) surface of cubic $ZrO_2$ (the interfacial oxygen atoms were common for the $ZrO_2$ and $MnO_2$ layers, i.e., some “spare” surface oxygen atoms were eliminated). Only the positions of zirconium and oxygen atoms in the lower $ZrO_2$ layer were fixed while all the other atoms were allowed to relax.

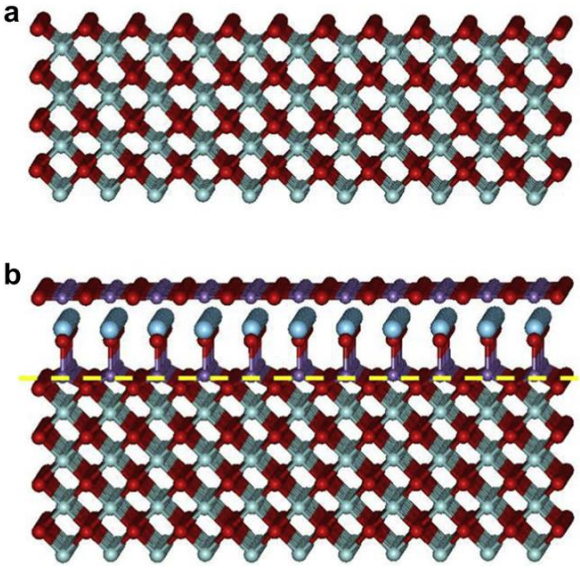


Figure 1.14 Atomic-scale models for YSZ surface and LSM/YSZ interface: (a) a free (001) surface for oxygen saturated stabilized cubic $ZrO_2$ structure; (b) a smooth $LaMnO_3/ZrO_2$ interface with (001) orientation. Oxygen atoms are shown in red, Zr - in small light blue balls, La - in big cyan balls, Mn - in purple. Only three layers of $LaMnO_3$ perovskite (nearest to the interface) are shown [43].

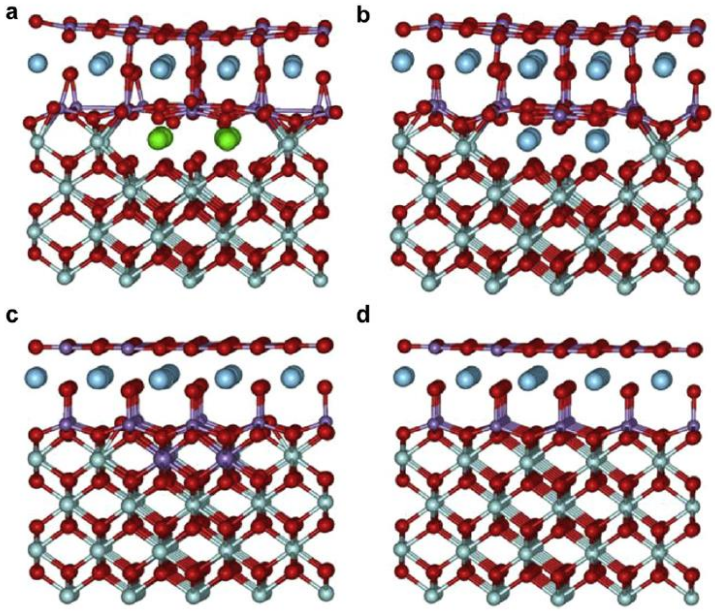


Figure 1.15 - Schematics for substitutional Sr (a), and La (b), and Mn (c) impurity defects in subsurface area of YSZ near the LSM/YSZ interface. A whole row of Zr atoms in the supercell was substituted by impurities. A defectless interface is shown for comparison (d). Oxygen atoms are shown in red, Zr - in small light blue balls, La e in big cyan balls, Mn e in purple, Sr - in green. Only three layers of $LaMnO_3$ perovskite (nearest to the interface) are shown. La-O and Sr-O bonds were omitted in figures (a) and (b) for better illustration [43].

As Fig. 1.15 shown, La and Sr metal impurities migrating across the interface into the electrolyte may significantly change the YSZ local structure near the interface (substitution of one $Zr4^{+}$ by $Sr2^{+}$ requires one oxygen vacancy to be introduced in the supercell). In particular, these large atoms generate a significantly larger distortion in the electrolyte network than Mn impurities simply because the La-O and Sr-O atomic bonds are longer than the Zr-O and Mn-O bonds which cause increased local strain in the electrolyte network.

Although Mn dopants do not produce any significant damage to the LSM/YSZ interface (like La and Sr atoms, see Fig. 15c), Mn is mixed valence transition-metal, and its accumulation within the electrolyte in the vicinity of the interface may significantly increase the electronic conductivity (e.g., through the $Mn3^{+}$-$Mn4^{+}$ transitions) This phenomenon may cause a premature conversion of oxygen ions $O^{2-}$ to neutral oxygen atoms in the electrolyte, and subsequently, into $O_2$ molecules that may be accumulated within voids and other defects, develop pressure, and eventually, accelerate crack formation.

Closed voids should be the main type of extended defects where gas pressure could be developed and cause the void growth and crack formation at interface.

## 1.4 Overview of SOFC degradation phenomena and mechanisms analysis: electrode

The degradation of SOFCs can be classified into two types—intrinsic (due to internal factors) and extrinsic (due to external factors). The intrinsic degradation includes microstructural changes, fractures, and delamination while extrinsic factors include reaction with components present in the fuel and the atmosphere. Corrosion is an extrinsic phenomenon which occurs due to various reasons affecting the performance of the cell. The materials constituting the electrodes and electrolyte is a major factor of corrosion. These materials and the design of the cells have been reviewed in great detail in the previous review paper [44]. Some factors of corrosion have been addressed in Fig. 1.16.

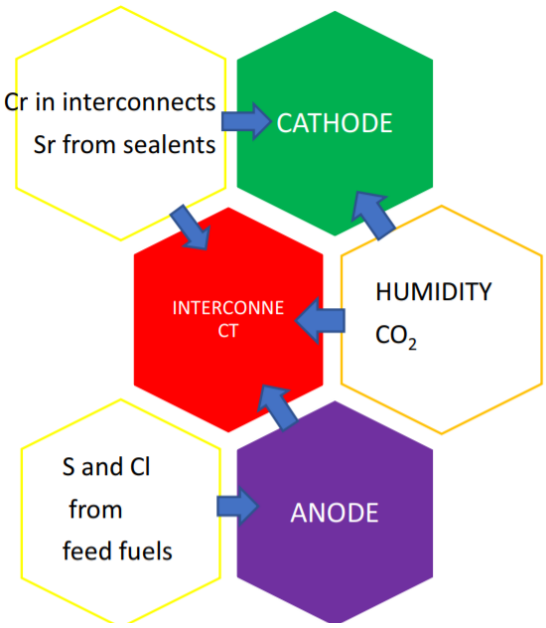


Figure 1.16 Factors affecting the performance of SOFCs [45]

### 1.3.1 Degradation phenomena and mechanisms of anodes:

For Ni–YSZ anodes, degradation mechanisms have been classified into three types: (1) material transport mechanisms (2) deactivation and passivation mechanisms and (3) thermomechanical mechanisms [46]. Material transport mechanism includes different microstructural changes due to the movement of Ni or impurity particles. It is most prominent type of anode degradation during which the Ni atoms, at higher temperatures, agglomerate by diffusion or by transport in gas phase [47,48,49,50]. Similarly, chemical gradients can develop due to the presence of impurities or unsuitable material combination, which in turn will affect the transport of particles throughout the microstructure [51, 52]. Deactivation and passivation mechanism is responsible for the performance loss due to the presence of impurities in carbonaceous fuels. Impurities mostly responsible for the faster degradation of Ni–YSZ anode are carbon and sulfur, hence the degradation processes are also termed as Coking [53] and Sulfur poisoning. During coking, carbon particles are formed by the Boudouard reaction. These particles settle on the Ni particles and inhibit the electrochemical reactions. Similarly, the presence of sulfur in fuel, in the form of $H_2S$, has also been found to be detrimental to the Ni particles [54,55]. $H_2S$ reacts with $O_2$ to release $H_2O$ and S. This S then settles down on the active sites and at the SOFC operating temperatures, $Ni_3S_2$ may form by the reaction between Ni and S. This is a volatile compound which will result in a reduction of Ni content on the anode side. The third type i.e. degradation by the thermomechanical mechanism includes the deterioration of the anode due to

the residual stresses, either between the interfaces at small scale or due to stack parameters at the large scale [46,56,57,58].

- **Nickel (Ni) coarsening**

One of the most common and dominant type of degradation which can be observed in Ni–YSZ anode after operation is Ni coarsening. The phenomenon is associated with the agglomeration of Ni, loss of Ni–Ni contact and change of surface morphology of Ni grains [59,60,61,62]. This coarsening of the Ni grains has been attributed to two mechanisms (1) Diffusion/ Sintering of particles, vacancies or grain boundaries and (2) Ni transport in gas phase [37,47]. Both these mechanisms highly depend upon the operating conditions of anode such as temperature and humidity, especially.

- **Sulfur poisoning**

One of the main challenges for the commercialization of SOFCs is to use commercially available fossil fuels. However, several impurities present in these fuels restrict their use in SOFC technology because of their damaging nature. Among these, Sulfur is an important constituent, which can either be an impurity or an additive in several fuels commercially available, present usually in the form of $H_2S$ [55]. The different sulfur compounds are known to interact with the Ni–YSZ anode in such a manner that polarization losses become dominant because they block the fuel supply to the system. Several studies [54,63,64] have shown that even few ppm of $H_2S$ can be detrimental to the Ni–YSZ anodes. It has been found that $H_2S$ is associated with a sharp decrease of voltage during the initial few hours followed by a gradual and slow deterioration of the cell [64,65]. Another study by Li et al. [66] shows that $H_2S$ poisoning is associated with blocking the migration of $O_2$ ions towards the TPBs. It is also responsible for blocking the fuel from travelling towards the active sites thus increasing polarization resistance [67, 68]. Moreover, $Ni_3S_2$ once formed, cannot be recovered and therefore, it is responsible for the permanent damage to the cell [66].

- **Coking**

An increase in the use of hydrocarbons for SOFCs has opened various research areas. These include modification of the microstructures of different components, identification of various problems arising during the long term use of these fuels and replacement of conventional ones with the newly developed more efficient materials. For state of the art Ni–YSZ anode, apart from sulfur poisoning, another phenomenon responsible for the degradation in the cell performance has been observed commonly known as coking.

Carbon formation or coking on porous materials is a result of different reactions and can produce different forms of carbon ranging from graphite to

high molecular weight hydrocarbons [69]. Carbon is thought to be accumulating in different ways. It can be present as (1) chemisorbed or physically adsorbed specie blocking the flow of fuel, or (2) surround the particle as a whole thus deactivating it completely or (3) can build its filaments that can induce stress and finally cracking in the material.

It is widely accepted that on metal supported catalysts, hydrocarbons dissociate to produce Cα, an adsorbed atomic carbon, formed at 200–400 °C. This Cα reacts with oxidant to form CO. However, excessive Cα, which does not get converted to CO, can result in the formation of Cβ, a polymeric form with a formation temperature of 250–500 °C. Similarly, fibers or whiskers (Cv) and graphitic carbon (Cc) are produced at a temperature range of 300–1000 °C and 500–550 °C, respectively. β and graphitic carbon can results in the formation of continuous film around the catalysts resulting in its deactivation while whiskers or fiber (Cv) formation causes the breakdown of the catalysts. These different forms of carbon and degradation mechanisms related to these have been described in detail in [70].

Carbon formation in these different forms can take place on Ni–YSZ anodes through dissolution–precipitation mechanism [71,72] in which C atoms dissolve into the Ni grains, diffuse through them and then get deposited at their outer surface. Similarly one other mechanism is the dissolution of carbon in the Ni grains which results in significantly changed dimensions of samples and results in the cracks in the cells [73]. The deposition, sometimes, is also associated with a phenomenon known as “metal dusting”, in which Ni becomes dust [74]. The deposition results in catalyst deactivation by covering the active sites which ultimately results in performance degradation.

### 1.3.2 Degradation phenomena and mechanisms of cathodes

Cathodes are exposed to humid air during long-term processes and are constantly corroded by $CO_2$ in the cell storage and working conditions. This has resulted in the cathode getting delaminated from the electrolyte. Apart from these external agents, Cr present in the interconnect alloys may likewise contaminate the cathode. Impurities present in the sealants, similar to Si, have been seen to poison the cathode by reacting with it and prevent the surface reactions from taking place [75,76,77].

- **$CO_2$ poisoning**

Adsorption of carbon dioxide on the perovskite surface causes the formation of carbonates. Strontium carbonate phases have been observed on the LSCF ($La_xSr_{1-x}Co_yFe_{1-y}O_{3-\delta}$) surface [77]. Zhao et al. [75] demonstrated that the adsorption followed Temkin model for the LSC ($La_{1-x}Sr_xCoO_{3-\delta}$) cathode in 550–650 °C and Freundlich model in 700–800 °C. In 650– 800 °C, it followed

the Freundlich model for the LSM ($(La_{1}–xSr_{x})1−yMnO_{3}$) cathode [65, 64]. Auger electron spectroscopy (AES) and attenuated total reflectance-Fourier transform infrared spectroscopy (ATR-FTIR) techniques have shown the formation of SrCO3 at the LSM surface by the following mechanism [76,78].

$$SrO(s) + CO_2(g) \rightarrow 4SrCO_3(s) \quad (1\text{-}9)$$

$CO_2$ poisoning led to an increase in polarization of the cathode as well as difficulty in adsorption of $O_2$. The degree of poisoning relied upon the nature of the B-site atom of $LaBO_3$. The impact of poisoning could be alleviated by the incorporation of Si in the perovskite material. This, nonetheless, had the disadvantage of silicon poisoning. The LSCF and LSC cathodes were seen to be comparatively tolerant at higher temperatures [75].

- **SrO segregation and generation of $Mn_3O_4$**

For the LSM cathode, there occurred SrO segregation and generation of $Mn_3O_4$ superficially, while $La_2Zr_2O_7$ and $Mn_2O_3$ were formed at the LSM/YSZ interface [79]. Liu et al. [80] showed that the LSM cathode was more susceptible than the LSCF cathode. There occurred a severe voltage drop and increment in non-ohmic resistance [79].

Volatile $Sr(OH)_2$ may be formed while operating the SOFC and transported through gas-phase evaporation and deposition, leading to Sr depletion on the perovskite material and subsequently lowering the cathode performance. Such volatile species have been seen to interact with the $ZrO_2$-based electrolytes and form $SrZrO_3$ precipitates. Temperature, humidity, and SrO activity has shown to influence the phenomena. However, this could be reduced by using, between the electrolyte and the cathode, a layer of GDC oxide diffusion barrier, which aids in Sr retention and suppresses the formation of $SrZrO_3$ [55].

- **Sulfur poisoning**

In sulfur poisoning mechanism, $SO_2$ occupies the oxide ion vacancies and a nucleation reaction occurs on the surface of the perovskite bringing about the formation of $SO_3^{2-}$ [81,82]. This was seen to be followed by the formation of $SrSO_4$ phase [83,84,85] at high temperatures (approximately ≥ 700 °C) and SrS phase at low temperatures (i.e., < 700 °C) [86,87]. A proposed mechanism [**Error! Bookmark not defined.**]:

$$10/3(La_{0.6}Sr_{0.4})(Co_{0.2}Fe_{0.8})O_3 + 13/3SO_2 + 5/3O_2 \rightarrow 4/3SrSO_4 + 2/3CoFe_2O_4 + La_2(SO_4)_3 + 2/3Fe_2O_3 \quad (1\text{-}10)$$

The corrosion effect was seen on both, the surface, as well as the bulk of the electrode as the exchange and diffusion processes for the oxygen reduction reaction on the surface was degraded, as shown in Fig. 1.17 [88].

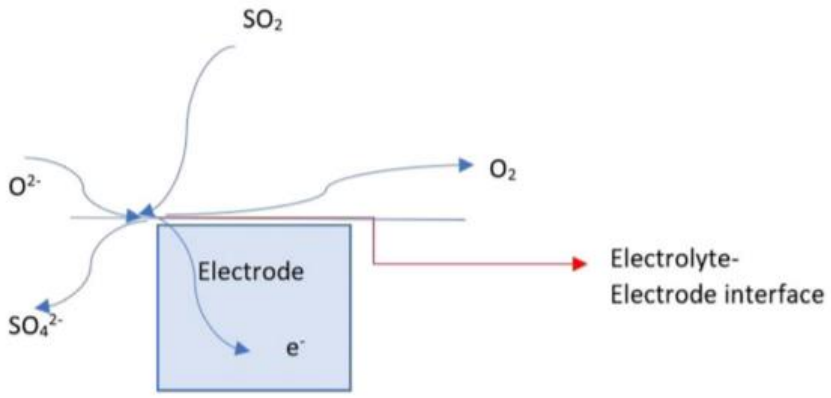


Figure 1.17 Schematic for sulfur poisoning at the electrode/electrolyte interface in SOFC [88]

- **Cr poisoning**

Chromium poisoning initiated from chromium-forming alloy interconnects [89,90,91,92]. Hilpert et al. [93] indicated that $CrO_3$ was the dominant species with dry air and $CrO_2(OH)_2$ with humid air [48]. It is not an electrochemical reaction in competition with $O_2$ reduction, [94] as had been anticipated by Taniguchi et al. It is a chemical process [95,96] kinetically controlled by the nucleation reactions [90,97,98], wherein deposition of Cr was seen on the surface of the cathode (in case of LSCF [99], LSCO ((La,Sr) $CoO_3$) [100,101], LSMC ($(La_{0.8}Sr_{0.2})0.95(Mn_1$-$xCo_x)O_3\pm d$) [102], and LSF ($La_{0.8}Sr_{0.2}FeO$) [103] electrodes) or the interface between the electrode and electrolyte (in the case of LSM ($LaSrMnO^{5+}$ δ) [95] and LNF ($LaNi_{0.6}Fe_{0.4}O_3$) [104] electrodes).

### 1.3.3 Degradation phenomena of the TPB area

The durability of the SOFCs is important for their commercialization. An important factor influencing the durability of SOFCs is the TPB region, which must be stable and optimized. The use of SOFCs for long durations has been seen to cause the depletion of this TPB area due to microstructural changes.

At TPB, $O_2$ from the YSZ reacts with $H_2$ flowing through the pore to produce electron which is then transported to the external circuit by the Ni particle. Water vapors produced are also transported outside the anode through the porous network. Ni–YSZ anode is fabricated in such a way that a large number of TPBs, in other words, a large number of reaction sites are obtained [105,106,107]. A schematic of the anode during the SOFC operation is given in Fig. 1.18.

Chromia-containing deposits were seen to cover the electrochemically active sites at the triple phase boundaries [92,108,109].

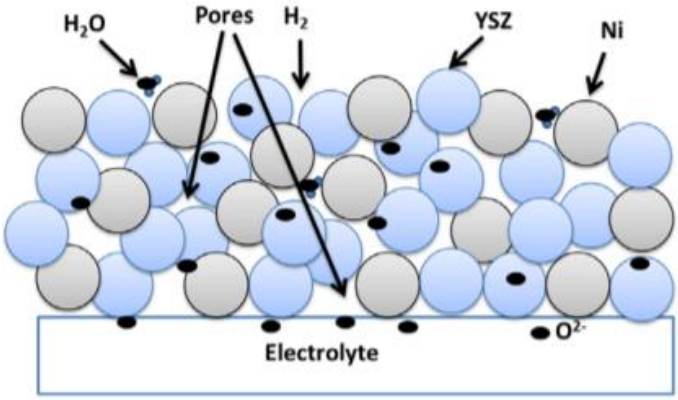


Figure 1.18 Schematic of Solid Oxide Fuel Cell Anode during operation [62]

## 2. Objectives of this thesis

- **Problems of SOEC degradation need to be solved**

SOEC degradation is often difficult to determine. The oxygen electrode material has a dominant role in the degradation of the SOEC. To date, the degradation mechanisms for the LSCF/LSM-based cathodes are ambiguous. Therefore, it is important to understand and address the reasons of degradation in SOECs.

Under anodic polarization, oxygen ion transports though the YSZ electrolyte via bulk and grain boundaries. The oxygen gas at the closed pores/cavities could diffuse into the air by redox reaction due to oxygen activity difference. The oxygen gas oxidized at the YSZ grain boundaries are accumulated at the closed pores/cavities of electrolyte of non-porous YSZ layer, resulting in the high oxygen pressure/activity at the electrode/electrolyte interface. The experiments cannot fully explain the electrochemical mechanism for the addition of porous layer. Thus, a model of the porous layer for electrochemical mechanism needs to be considered.

- **Problems of SOFC degradation need to be solved**

The interaction between metallic interconnect and cathodes of SOFCs has been extensively investigated in last 10–15 years and great deal of information is available. However, the chromium deposition and poisoning are a complex process because many interrelated factors, such as operating temperature, O2 partial pressure, air flow, direct or indirect contact with interconnect, applied current load, properties of electrolyte and composition and nature of electrode materials in particular, affect the amount, location and accumulation of chromium deposition.

Among other SOFC degradation phenomena, Cr poisoning is one of the most often mentioned degradation mechanisms in recent long-term stack tests.

## 2.1 Main contents of this thesis

Chapter 1: Research status of SOEC/SOFC technology is the main focus of this chapter. The main components and working principles of SOEC/SOFC are discussed. The overview of SOEC degradation phenomena and mechanism analysis at the electrode/electrolyte interfaces are given as the foundations and theoretical support for the work and investigations done in the next chapters. Additionally, some important issues of SOEC/SOFC degradation are addressed.

Chapter 3: Investigation of electrochemical equilibrium theory on SOEC/SOFC: The electrochemical equilibrium theory is introduced in the SOEC working condition to achieve simulations of electric potentials, electrochemical potentials of oxygen ions/molecules, oxygen partial pressure, local electronic conductivity, and total electronic area specific resistance of the electrolyte. Different theoretical cell designs were applied to the simulation to investigate the most optimized cell designs in terms of electrochemical performance.

Chapter 4: SOFC Chromium poisoning: A full explanation of the Cr poisoning mechanism is introduced. Among other interrelated factors, the investigation of the Chromium poisoning under different oxygen partial pressure is the major focus. Found the relation of oxygen partial pressure and Cr vaporization to reduce the Cr poisoning effect.

Chapter 5: Conclusions of electrochemical equilibrium theory and Chromium poisoning are presented.

## 3. Innovations of the SOEC electrochemical analysis influenced by oxygen partial pressure: Simulation of oxygen partial pressure and proposed improved micro-structure design

A MATLAB simulation based on the study of Zhang and Virkar [110] in 2019. The simulation is one-dimensional model made with functions of position, and different functions are used to distinguish n-type/p-type conductivity. The model can achieve simulations of electric potentials, electrochemical potentials of oxygen ions/molecules, oxygen partial pressure, local electronic conductivity, and total electronic area specific resistance of the electrolyte.

### 3.1 Electrochemical equilibrium model

Addition of the porous YSZ layer to the interface of the anode can reduce the degradation process of the SOEC. A porous YSZ layer is introduced to the interface of the anode. The $r_i^{el-p}$ is the ionic conductivity of the porous YSZ layer; The $r_i^{el-d}$ is the ionic conductivity of the regular (dense) YSZ electrolyte layer, as shown in Fig. 3.1 and Fig. 3.2.

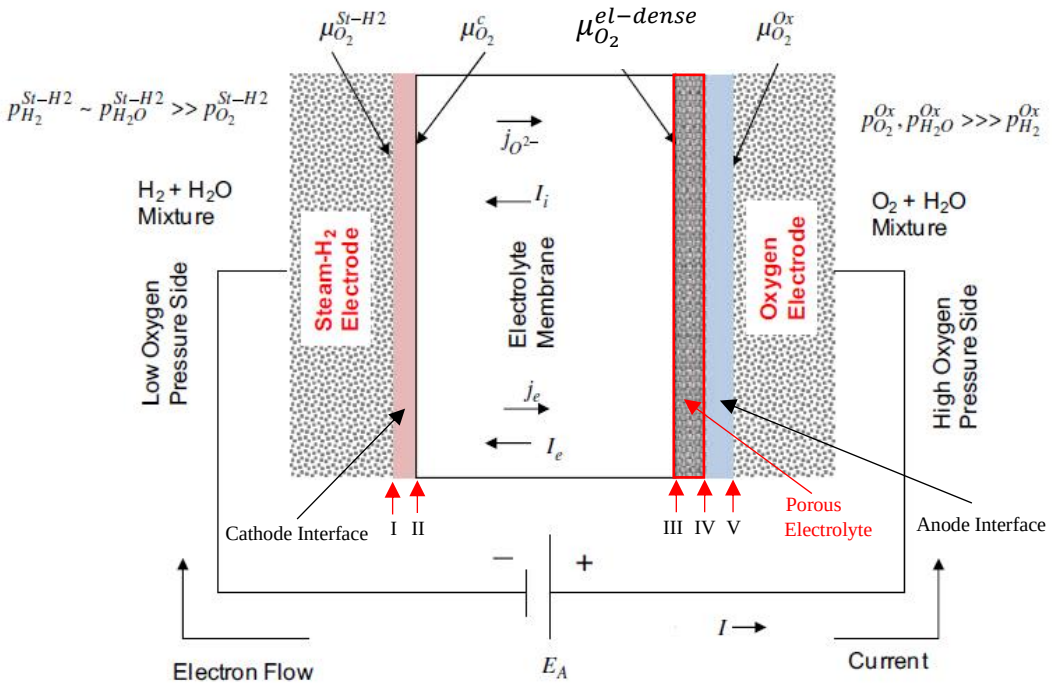


Figure 3.1 A schematic of a solid oxide electrolyzer cell, when operated in the electrolyzer mode ($E_A$>$E_N$). Steam-$H_2$ electrode is on the left; and oxygen electrode is on the right

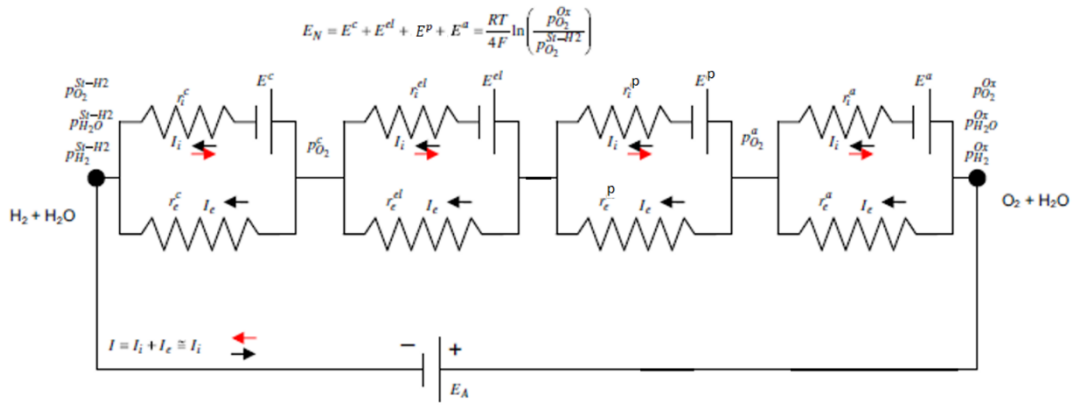


Figure 3.2 One dimensional model illustrating the layered structure of an SOEC

### 3.1.1 The layered structure and equivalent circuit of a porous YSZ SOEC

The interfaces between the cathode and the electrolyte and the anode and the electrolyte are very thin (nm). The figure shows finite width for the purposes of illustration. The changes in the various potentials at the interfaces are thus abrupt.

Fig. 3.2 is an equivalent circuit for the cell in a 'true' steady state with an externally applied voltage source, $E_A$. In Fig. 3.2, $r_i^c$ and $r_i^a$ are respectively the area specific ion charge transfer resistances at the steam-$H_2$ electrode/electrolyte interface and the oxygen electrode/electrolyte interface. In a 'true' steady state, electronic and ionic current densities are uniform through all segments of the equivalent circuit, that is $\rightarrow \nabla \cdot \vec{I_\iota} = 0$ and $\rightarrow \nabla \cdot \vec{I_e} = 0$. Thus in a true steady state, we must always have $\varphi^{Ox} > \varphi^a > \varphi^c > \varphi^p > \varphi^{St-H_2}$ (for the case, $\varphi^{Ox} > \varphi^{St-H_2}$ , selected here, that is for $E_A > 0$) where $\varphi$ is the electric potential.

In Fig 3.2, the positive directions of the ionic and the electronic currents are shown by arrows. In the fuel cell mode ($E_A < E_N$), the ionic current direction is shown by red arrows ($I_i > 0$). In the electrolyzer mode ($E_A > E_N$), the ionic current direction is shown by black arrows ($I_i < 0$). Thus, the sign of the ionic current depends upon the sign of $E_A - E_N$. For the cases considered here, $E_A > 0$. Thus, the electronic current through the cell is always negative ($I_e < 0$). Note that generally $|I_i| >> |I_e|$.

### 3.1.2 Thermodynamic and electrochemical equilibrium:

Two fundamental assumptions will be made. Local thermodynamic equilibrium exists as shown in equation (3-1). This means thermodynamic quantities are locally defined but global thermodynamic equilibrium may not exist. Local chemical equilibrium exists as shown in equation (3-2). This may

take a long period of time, especially at low temperatures. The former means, for a local reaction of the type local thermodynamic potentials are defined; that is the chemical potential of $O_2$, $\mu_{O_2}$, the electrochemical potential of electrons, $\tilde{\mu}_e$, and the electrochemical potential of oxygen ions, $\tilde{\mu}_{O^{2-}}$ are locally defined. However, it is possible that locally $\frac{1}{2}\mu_{O_2} + \tilde{\mu}_e > \tilde{\mu}_{O^{2-}}$ or $\frac{1}{2}\mu_{O_2} + \tilde{\mu}_e < \tilde{\mu}_{O^{2-}}$If it is the former, then locally the reaction goes forward (albeit may be very slowly). If it is the latter, the reaction goes backward. In either case, local thermodynamic equilibrium prevails but there is no local chemical equilibrium.

The mathematical model is made based on the local thermodynamic and chemical equilibrium with the assumptions above.

We will define, following Hebb [111]:

$$\varphi = -\frac{\tilde{\mu}_e}{e} = -\frac{\mu_e}{e} + \phi \tag{3-1}$$

where $\phi$ is the local electrostatic potential. Since the transporting species are oxygen ions and electrons/holes, in steady state we must have (for a one-dimensional problem)

$$\frac{d}{dx}\left(\sigma_i(x)\frac{d}{dx}(\tilde{\mu}_{O^2} - (x)\right) = 0 \tag{3-2}$$

where $\sigma_i(x)$ is the oxygen ion conductivity at distance x from the surface of the electrolyte, and

$$\frac{d}{dx}\left(\sigma_e(x)\frac{d}{dx}(\varphi(x))\right) = 0 \tag{3-3}$$

where $\sigma_e$ (x) is the local electronic conductivity.

Electronic conductivity depends on the local oxygen partial pressure or the chemical potential of oxygen and may be given as

$$\sigma_e(x) = f(\mu_{O_2}(x)) = f(4e\varphi(x) + 2\tilde{\mu}_{O^{2-}}(x)) \tag{3-4}$$

### 3.1.3 Electron and hole conductivities:

Electron and hole conductivities of 8YSZ as functions of temperature and oxygen partial pressure have been measured by Park and Blumenthal [112] given as

$$\sigma_e^{YSZ} = 1.32 \times 10^7 exp\left(-\frac{3.88}{k_B T}\right) p_{O_2}^{-\frac{1}{4}} \tag{3-5}$$

and

$$\sigma_h^{YSZ} = 2.35 \times 10^2 exp\left(-\frac{1.67}{k_B T}\right) p_{O_2}^{\frac{1}{4}} \tag{3-6}$$

Substituting Equations (3-5) and (3-6) into the electronic conductivity of the YSZ electrolyte as a function of position gives:

$$\sigma_h^{YSZ} = 1.32 \times 10^7 exp\left(-\frac{3.88}{k_B T}\right) p_{O_2}^{a\ -\frac{1}{4}} exp\left(-\frac{(\tilde{\mu}_{O^{2-}}(x) + 2F\varphi(x))}{2RT}\right) + 2.35 \times 10^2 exp\left(-\frac{1.67}{k_B T}\right) p_{O_2}^{a\ \frac{1}{4}} exp\left(\frac{(\tilde{\mu}_{O^{2-}}(x) + 2F\varphi(x))}{2RT}\right) \quad (3\text{-}7)$$

In the one-dimensional case, we have

$$\frac{d}{dx}\left[\sigma_e(x)\frac{d}{dx}\varphi(x)\right] = 0 \quad (3\text{-}8)$$

### 3.1.4 Second order differential equation:

In order to solve the second order differential equation using the Boundary Value Problem (BVP) solver, Equation (3-8) needs to be expressed using two first order differential equations defining:

$$y_1(x) \equiv \varphi(x) \quad (3\text{-}9)$$

$$y_2(x) \equiv \sigma_e(x)\frac{d}{dx}\varphi(x) \quad (3\text{-}10)$$

Therefore, the two first order differential equations are

$$\frac{d}{dx}y_1(x) = \frac{y_2(x)}{\sigma_e(x)} \quad (3\text{-}11)$$

and

$$\frac{d}{dx}y_2(x) = 0 \quad (3\text{-}12)$$

The boundary conditions are $y_1(0) = \varphi^{II}(r_e^{ele}), y_1(L) = \varphi^{III}(r_e^{ele})$,where II and III are the position showed in Fig. 2.1, $r_e^{ele}$ is given by equation (3-14).

However, $\varphi^{II}$ and $\varphi^{III}$ are coupled to the integration of electronic resistivity. Therefore, an additional differential equation is needed by defining:

$$y_3(x) \equiv \int_0^x \frac{dt}{\sigma_e(t)} \quad (3\text{-}13)$$

By definition, $y_3(x)$, is the cumulative electronic area specific resistance from the anode interface to a point x in the electrolyte. Thus, $y_3(L)$ is the total electronic ASR through the electrolyte. The boundary conditions are $y_1(0) = \varphi^{II}(y_3(L)), y_1(L) = \varphi^{III}(y_3(L))$ and $y_3(0) = 0$.

### 3.1.5 Other parameters' modeling:

- **electronic area specific resistance $\mathbf{r_e^{ele}}$**

  The $r_e^{ele}$ is electronic area specific resistance of the electrolyte is given by

$$r_e^{ele} = \int_0^L \frac{dx}{\sigma_{el}(x)} \quad (3\text{-}14)$$

- **Oxygen ion electrochemical potential $\tilde{\mu}_{O^{2-}}$**

The oxygen ion electrochemical potential in electrolyte adjacent to the anode interface $\tilde{\mu}_{O^{2-}}^{III}$ and position II are given by

$$\tilde{\mu}_{O^{2-}}^{II} = \tilde{\mu}_{O^{2-}}^{c} + \left(\tilde{\mu}_{O^{2-}}^{a} - \tilde{\mu}_{O^{2-}}^{c}\right)\left(\frac{r_i^c}{r_i^a + r_i^{el} + r_i^c + r_i^{el-p}}\right) \quad (3\text{-}15)$$

$$\tilde{\mu}_{O^{2-}}^{III} = \tilde{\mu}_{O^{2-}}^{c} + \left(\tilde{\mu}_{O^{2-}}^{a} - \tilde{\mu}_{O^{2-}}^{c}\right)\left(\frac{r_i^c + r_i^{el}}{r_i^a + r_i^{el} + r_i^c + r_i^{el-p}}\right) \quad (3\text{-}16)$$

$$\tilde{\mu}_{O^{2-}}^{IV} = \tilde{\mu}_{O^{2-}}^{c} + \left(\tilde{\mu}_{O^{2-}}^{a} - \tilde{\mu}_{O^{2-}}^{c}\right)\left(\frac{r_i^c + r_i^{el} + r_i^{el-p}}{r_i^a + r_i^{el} + r_i^c + r_i^{el-p}}\right) \quad (3\text{-}17)$$

Oxygen ion electrochemical potential is a linear function of position in the electrolyte shown below:

$$\tilde{\mu}_{O^{2-}}(x) = \begin{cases} \tilde{\mu}_{O^{2-}}^{II} + \left(\tilde{\mu}_{O^{2-}}^{III} - \tilde{\mu}_{O^{2-}}^{II}\right)\left(\frac{x}{L}\right) & x \le L_1 \\ \tilde{\mu}_{O^{2-}}^{III} + \left(\tilde{\mu}_{O^{2-}}^{IV} - \tilde{\mu}_{O^{2-}}^{III}\right)\left(\frac{x - L_1}{L - L_1}\right) & x > L_1 \end{cases} \quad (3\text{-}18)$$

where $L_1$ is the thickness of the dense YSZ electrolyte layer

- **Oxygen partial pressure $\mathbf{p_{O_2}}$**

The oxygen partial pressure at position x, $p_{O_2}(x)$, is related to the oxygen partial pressure at the anode,$p_{O_2}^a$, and at cathode $p_{O_2}^c$

$$p_{O_2}(x) = p_{O_2}^a exp\left(\frac{\mu_{O^{2-}}(x)}{RT}\right) \times p_{O_2}^c \quad (3\text{-}20)$$

where $\mu_{O^2}(x) = 4e\varphi(x) + 2\tilde{\mu}_{O^{2-}}(x)$

- **Nernst voltage $E_N$:**

The applied voltage $E_A$ is in the opposite direction to the Nernst voltage $E_N$ created by differing oxygen partial pressures at the two electrodes; that is, the positive of the cell is connected to the positive of the external source and the negative of the cell is connected to the negative of the external source. When $E_A < E_N$, the cell does work on the external source
(charging the externally connected battery). This is the fuel cell mode. When $E_A > E_N$, the external source does work on the cell. This is the electrolyzer mode. The Nernst voltage generated by differing oxygen partial pressures at the two electrodes is given by:

$$E_N = \frac{RT}{4F} ln\left(\frac{P_{O_2}^{Ox}}{P_{O_2}^{St-H_2}}\right) \quad (3\text{-}21)$$

However, other research paper [29] addressed the Nernst voltage can be affected not only by oxygen partial pressures but also the humidity of the steam and flowrate of the air, etc.

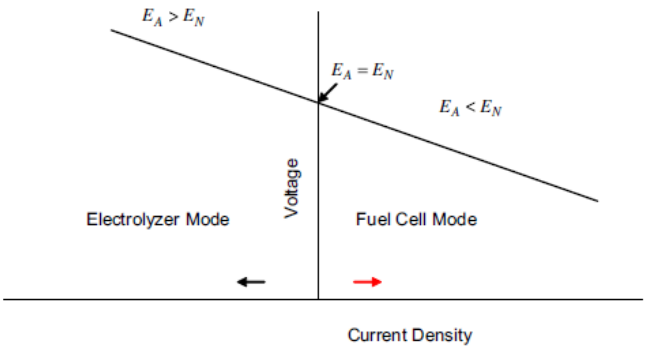


Figure 3.3 A schematic plot of the measured voltage (which is also the applied voltage, $E_A$) vs. the measured current density [29].

## 3.2 Simulation of SOEC operation and verification

### 3.2.1 Model Validation: Model without porous electrolyte layer

Simulation parameters: For a real SOEC, the boundary conditions are determined by the working conditions. The cell is assumed to operate at 800°C. The partial pressure of oxygen at the cathode (fuel side in SOEC) is set at $p_{O_2}^c$ = $10^{-20}$ atm and the partial pressure of oxygen at the anode side (oxygen electrode) is set at $p_{O_2}^a$ = 1 atm. The applied potential $E_A$ is 1.5 V, this correspond to a Nernst voltage $E_N$ = 1.0645 V. Therefore, $\frac{\mu_{O_2}^c}{4F}$ = 0 V, $\frac{\mu_{O_2}^a}{4F}$ = 1.0645 V, $\varphi^c$= 0 V, and $\varphi^a$ = 1.5 V. All of the simulation parameters are listed in Table I form Zhang and Virkar's research [110].

The total oxygen ion electrochemical potential $\tilde{\mu}_{O^{2-}}$, is a linear function of position in the electrolyte.

$$\tilde{\mu}_{O^{2-}}(x) = \begin{cases} -0.056 \times \left(\frac{x}{L}\right) \times 2F & x \le L_1 \\ -0.056 \times \left(\frac{x - L_1}{L - L_1}\right) \times 2F & x > L_1 \end{cases} \quad (3\text{-}22)$$

Table 1 Simulation Parameters [100]

| Electrolyte Units | Electronic ASR Cathode (fuel electrode) Interface $\Omega cm^2$ | Electronic ASR Electrolyte | Electronic ASR Anode (oxygen electrode) Interface $\Omega cm^2$ | Anode $p_{O_2}$ atm | Cathode φ V | Ionic ASR Electrolyte $\Omega cm^2$ |
|---|---|---|---|---|---|---|
| YSZ-1 | 0 | Park | 1.5 | 1 | -1.5 | 0.044 |
| YSZ-5 | 0 | Park** | 1.5 | 1 | -1.5 | 0.044 |
| YSZ-6 | 0 | Park*** | 1.5 | 1 | -1.5 | 0.044 |
| Electrolyte Units | Ionic ASR Anode (oxygen electrode) Interface $\Omega cm^2$ | Temperature °C | Ionic ASR Cathode (fuel electrode) Interface $\Omega cm^2$ | Cathode $p_{O_2}$ atm | Anode φ V | N-type Electronic Conductivity |
| YSZ-1 | 0.3 | 800 | 0 | $10^{-20}$ | 0 | 1 (time) |
| YSZ-5 | 0.3 | 800 | 0 | $10^{-20}$ | 0 | 1000 (time) |
| YSZ-6 | 0.3 | 800 | 0 | $10^{-20}$ | 0 | 2000 (time) |

### 3.2.2 Results and discussions

The calculated results for YSZ-1 cell, YSZ-5 cell and YSZ-6 cell are shown in Fig. 3.4, Fig.3.5 and Fig. 3.6, respectively.

This is a numerical theoretical validation based on the study of thermodynamic and electrochemical equilibrium without the porous electrolyte in order to compare with the results from the work of Zhang and Virkar [100]. The simulation is one-dimensional model made with functions of position, and different functions are used to distinguish n-type/p-type conductivity. The model can achieve simulations of electric potentials φ, electrochemical potentials of oxygen ions $\mu_{O_{2-}}$ and molecules $\mu_{O_2}$, oxygen partial pressure $p_{O_2}$, local electronic conductivity, and total electronic area specific resistance of the electrolyte. The results in Fig. 3.6 show good agreement with Fig. 3.7 in reference [100]. It proves the reliability of the electrochemical equilibrium model and the numerical simulation.

In YSZ-1 cell, the electronic resistance of the electrolyte, $r_e^{el}$, is much larger than $r_a^e$ and $r_c^e$. Therefore, most of the electrical potential, φ, drops through the electrolyte. However, the ionic resistance associated with the oxygen electrode, $r_i^e$, is much larger than the fuel electrode interface resistance (which is assumed to be zero) and the electrolyte ionic resistance. As a result, most of the electrochemical potential of oxygen ions drops across the electrolyte/oxygen electrode interface.

In order to simulate the influence of adding some $CeO_2$ to YSZ, the pre-exponential factor in the electron conductivity for YSZ-5 and YSZ-6 is multiplied

respectively by 1000 and 2000. All other parameters were maintained the same as YSZ-1. Fig. 3.5 shows the results for YSZ-5 cell with higher electron conductivity. Approximately, 93% of the electrolyte thickness is n-type. As a result, the oxygen pressure is below 100 atm through much of the thickness. In such a scenario, electrolyte cracking is unlikely, but oxygen electrode delamination could still occur. The ionic current density is 1.27 $Acm^{-2}$ but the electronic current density is 0.1 $Acm^{-2}$. The corresponding membrane ionic transference number is 0.9217. Fig. 3.6 shows the calculated results for YSZ-6 cell. The electric potential, the oxygen partial pressure and the electronic conductivity are concave up through the entire thickness of the electrolyte. The maximum oxygen partial pressure is limited to 1 atm, and no cracking or oxygen electrode delamination is expected. The ionic current density is 1.27 $Acm^{-2}$ and the electronic current density is 0.21 $Acm^{-2}$. The corresponding membrane ionic transference number is 0.858. Thus, the electronic leakage is substantial. In concept, however, it is possible to operate a leaky SOEC at some different operating points such that one can effectively led to the same efficiency as an SOEC made of purely oxygen ion conducting electrolyte.

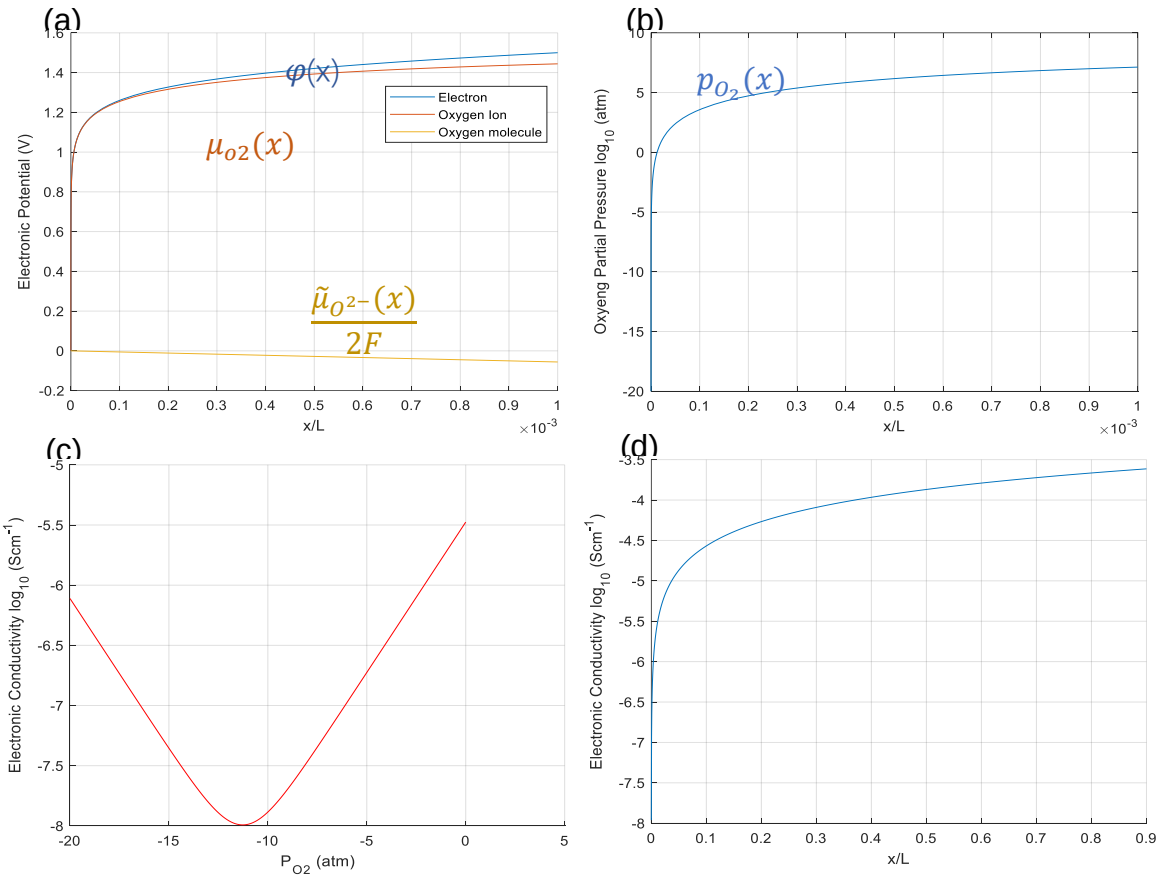

Figure 3.4 Calculated results for YSZ-1 cell (a) Plots of $\varphi$(x), $\frac{\tilde{\mu}_{O^{2-}}(x)}{2F}$, $\frac{\mu_{o2}(x)}{2F}$, in the electrolyte. (b) Plots of oxygen partial pressure as a function of distance in the electrolyte. (c) Electronic conductivity as a function of oxygen partial pressure. (d) The blue curve is the electronic conductivity in the electrolyte as a function of distance from the cathode/electrolyte interface

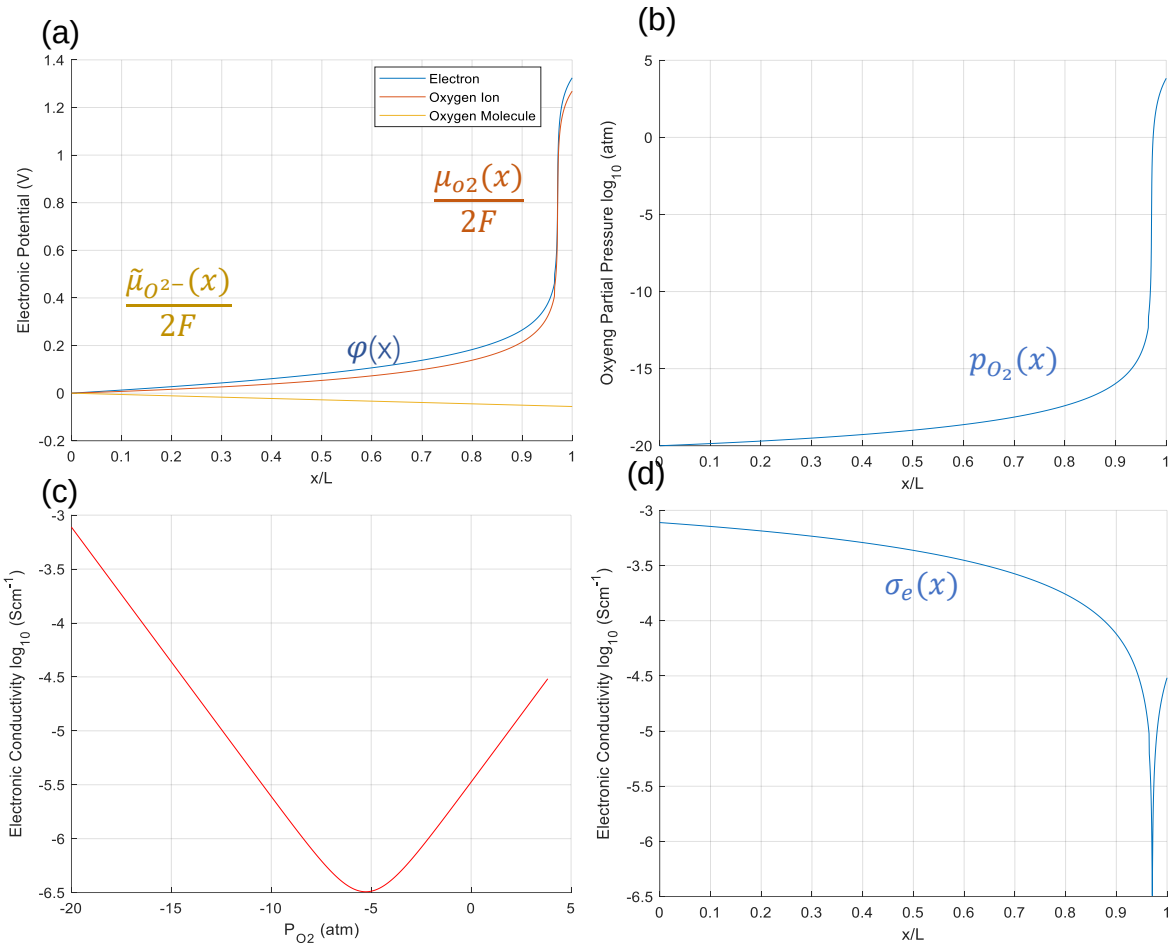


Figure 3.5 Calculated results for YSZ-5 cell. (a) Plots of $\varphi$(x), $\frac{\tilde{\mu}_{O^{2-}}(x)}{2F}$, $\frac{\mu_{o2}(x)}{2F}$, in the electrolyte. (b) Plots of oxygen partial pressure as a function of distance in the electrolyte. (c) Electronic conductivity as a function of oxygen partial pressure. (d) The blue curve is the electronic conductivity in the electrolyte as a function of distance from the cathode/electrolyte interface

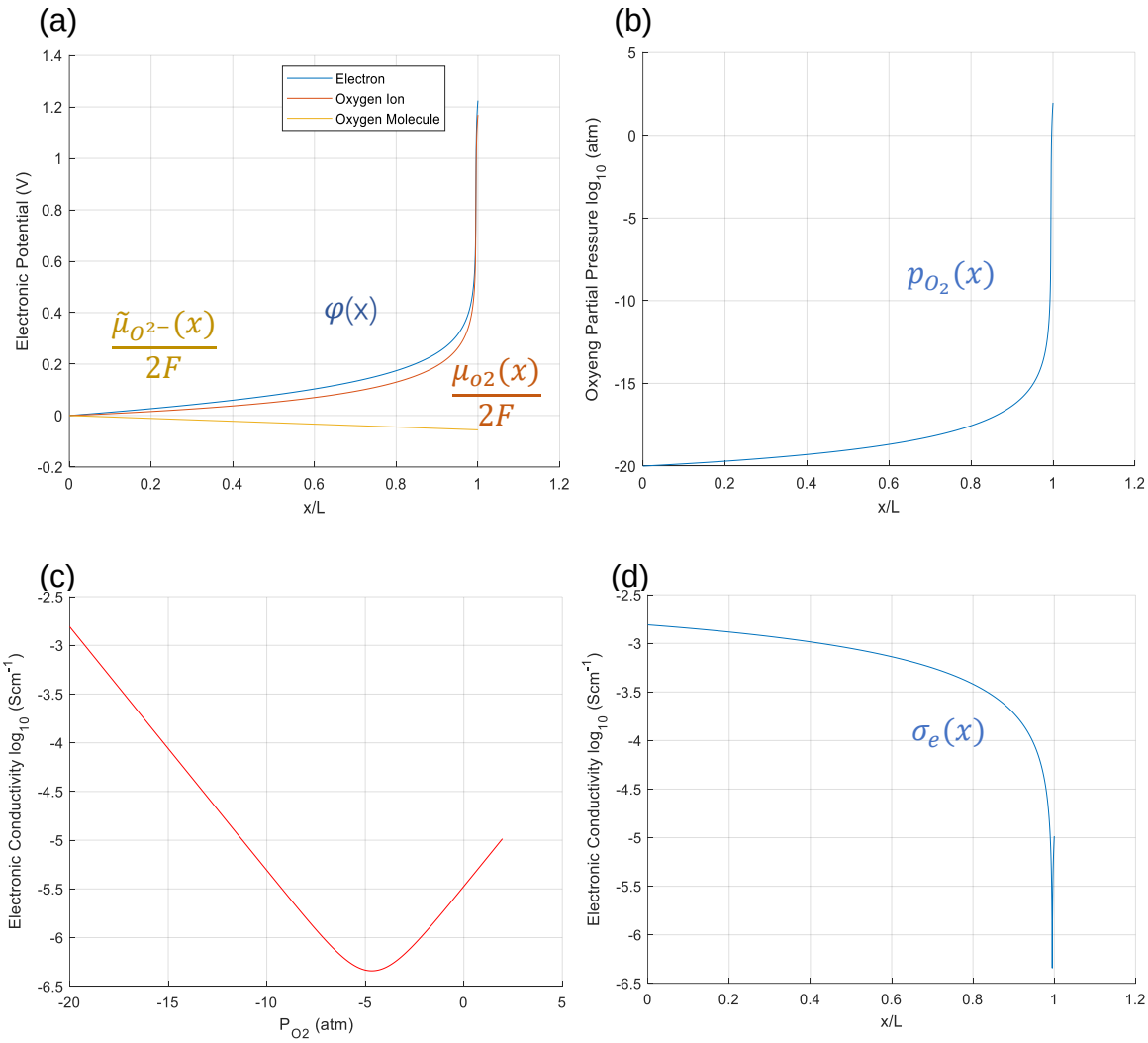


Figure 3.6 Calculated results for YSZ-6 cell. (a) Plots of $\varphi$(x), $\frac{\tilde{\mu}_{O^{2-}}(x)}{2F}$, $\frac{\mu_{o2}(x)}{2F}$, in the electrolyte. (b)Plots of oxygen partial pressure as a function of distance in the electrolyte. (c) Electronic conductivity as a function of oxygen partial pressure. (d) The blue curve is the electronic conductivity in the electrolyte as a function of distance from the cathode/electrolyte interface

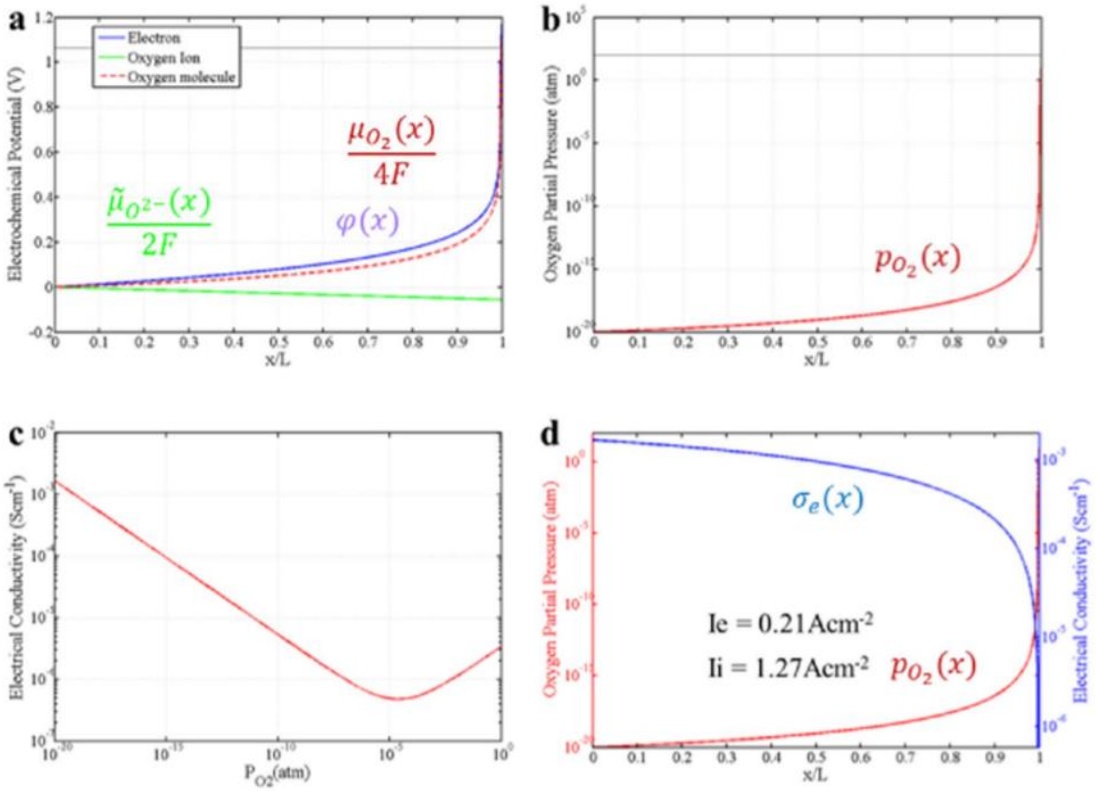


Figure 3.7 Reference's results for YSZ-6 cell [110]. (a) Plots of $\varphi$(x), $\frac{\tilde{\mu}_{O^{2-}}(x)}{2F}$, $\frac{\mu_{O2}(x)}{2F}$, in the electrolyte. (b)Plots of oxygen partial pressure as a function of distance in the electrolyte. (c) Electronic conductivity as a function of oxygen partial pressure. (d) The blue curve is the electronic conductivity in the electrolyte as a function of distance from the cathode/electrolyte interface

## 3.3 Model with a porous electrolyte layer to increase the cell efficiency

### 3.3.1 SOEC parameters with a porous electrolyte layer

By considering the diffusion path of the oxygen ion at the electrolyte/anode interface, YSZ porous layer was prepared on both sides of YSZ electrolyte to prevent the delamination of the interface. The oxygen gas at closed pores/cavities at the solid-solid two-phase (oxygen electrode and electrolyte) interface could diffuse rapidly into air [35,16].

The stack temperature is kept at 800 $^{o}$C. The gas flow rates are kept constant during the electrolysis operation as 4.5 Nl/min $H_2$ and 4.5 Nl/min $H_2O$ at fuel side and 16 Nl/min air. The current density is kept at -0.5 Acm$^2$ during electrolysis operation, which corresponds to a steam conversion rate of 50%. The Nernst voltage $E_N$ is 0.935 V. The following cell configuration and working condition are from the Yan's experiments [113], shown in Tab. 2.

Table 2 Cell configuration and working condition

| Cell configuration | Electrolyte thickness (μm) | Operation temperature (˚ C) | Ionic ASR Cathode (fuel electrode) Interface ($\Omega cm^2$) | Ionic ASR Electrolyte ($\Omega cm^2$) | Ionic ASR Anode (oxygen electrode) Interface ($\Omega cm^2$) |
|---|---|---|---|---|---|
| Cell 1 | 10 | 800 | 0 | 0.044 | 1.93 |
| Cell 2 | 2 | 800 | 0 | 0.0088 | 1.40 |

### 3.3.2 Results and discussions

The results from the model with a porous electrolyte layer are shown in Fig. 3.8 and Fig. 3.9. The oxygen partial pressure at the interface adjacent to the anode is obtained as 0.39 atm for Cell 1 and 0.42 atm for Cell 2 at the current density being -0.5 $Acm^2$, still larger than oxygen partial pressure in air, meaning that certain amount of oxygen gas accumulates closed pores/cavities of the electrolyte. Delamination due to high partial pressure of oxygen is less likely to occur. This working condition of the cells is acceptable in real engineering.

It may be predicted that the efficiency of the cells may be increased significantly if the current density is increased a little such as the current density being -0.6 $Acm^2$ during electrolysis operation. It is a regular current density used in SOEC.

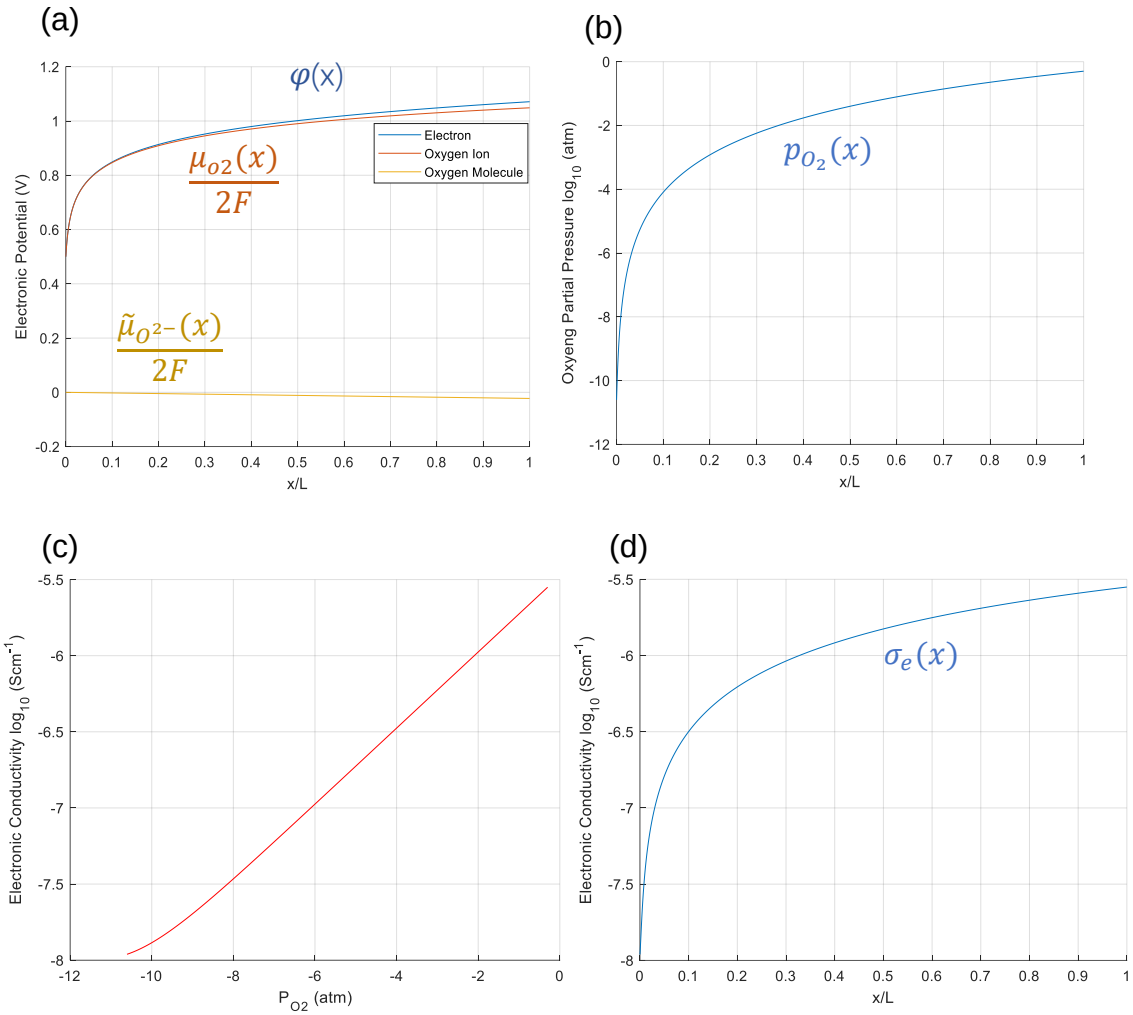


Figure 3.8 Calculated results for cell 1. (a) Plots of $\varphi$(x), $\frac{\tilde{\mu}_{O^{2-}}(x)}{2F}$, $\frac{\mu_{o2}(x)}{2F}$, in the electrolyte. (b) Plots of oxygen partial pressure as a function of distance in the electrolyte. (c) Electronic conductivity as a function of oxygen partial pressure. (d) The blue curve is the electronic conductivity in the electrolyte as a function of distance from the cathode/electrolyte interface

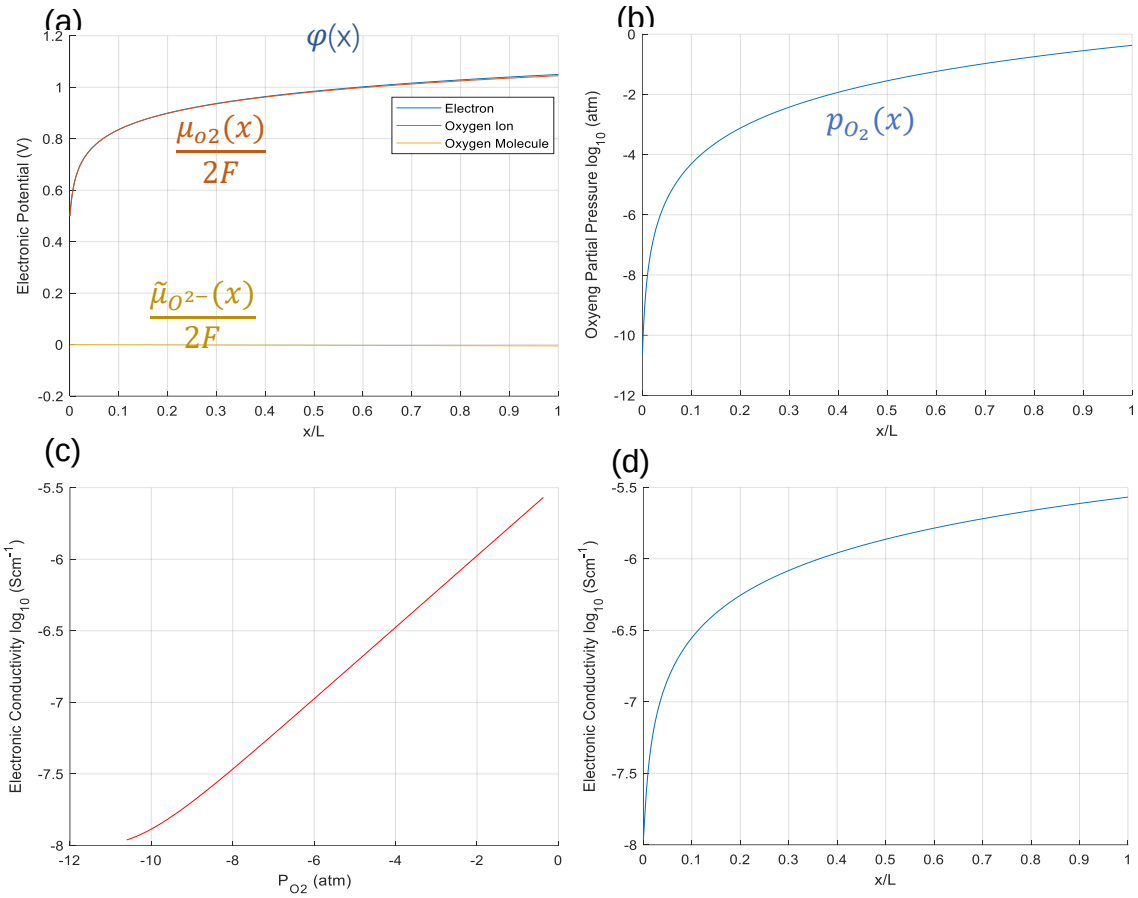


Figure 3.9 Calculated results for cell 2. (a) $\varphi$(x), $\frac{\tilde{\mu}_{O^{2-}}(x)}{2F}$, $\frac{\mu_{o2}(x)}{2F}$, in the electrolyte. (b) Oxygen partial pressure as a function of distance in the electrolyte. (c) Electronic conductivity as a function of oxygen partial pressure. (d) The blue curve is the electronic conductivity in the electrolyte as a function of distance from the cathode/electrolyte interface.

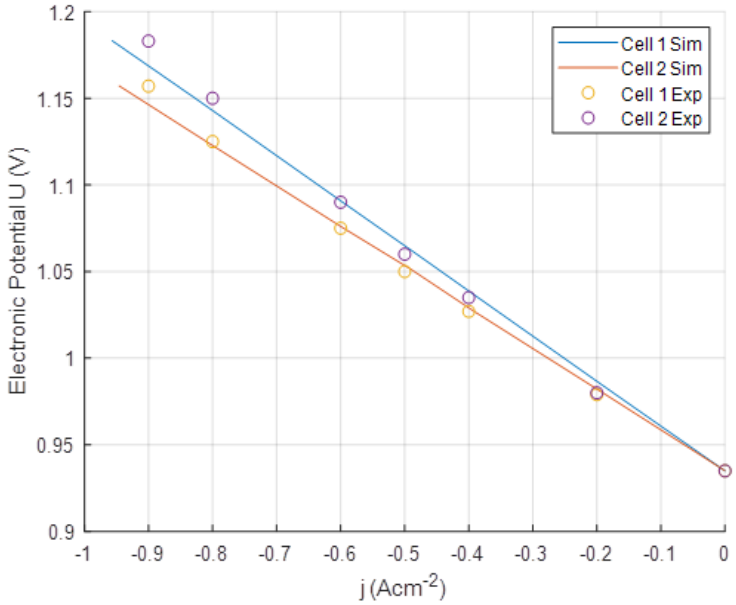


Figure 3.10 Comparison of the I-V curve between the experimental measurements [113] and the simulation in the paper in SOEC modes during the stationary operation.

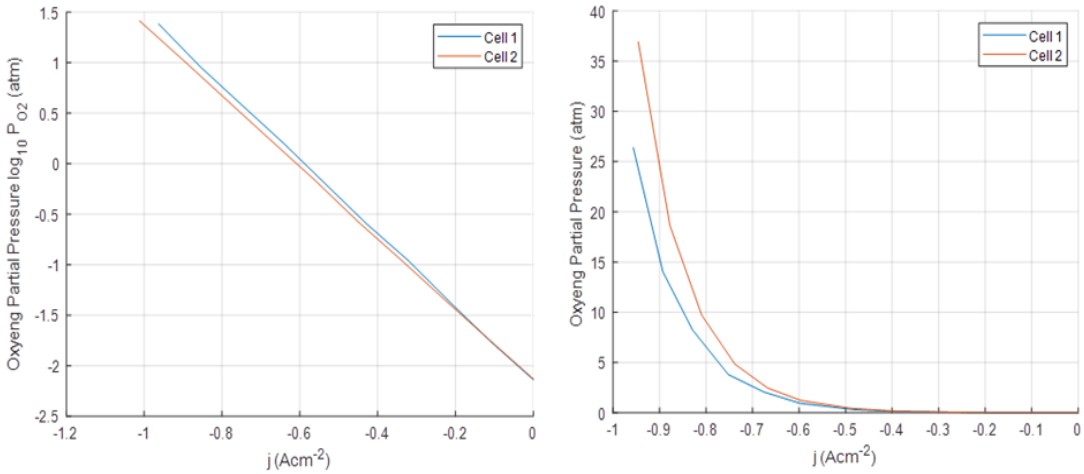


Figure 3.11 Plots of oxygen partial pressure at the interface adjacent to the anode as a function of the current density in the electrolyte in SOEC modes

In Fig. 3.10 the I-V curve simulated by the model in the paper is compared with the experimental measurements [113] in SOEC modes during the stationary operation. The simulation result shows good agreement with the experimental result.

Fig. 3.11 is the oxygen partial pressure at the interface adjacent to the anode as a function of the current density in the electrolyte in SOEC modes. It is found

that the oxygen partial pressure at the interface increases violently with the increase of the current density (when the current density reaches -0.6 $Acm^2$.

### 3.3 Improved electrode/electrolyte interfacial micro-structure design of SOEC

In order to analyze the influence of interface microstructure parameters on cell performance, such as porous layer porosity, thickness, Nernst voltage and interfacial resistances, etc., these parameters are studied separately to find reasonable interface porous layer parameters and provide reference for the design of the interfacial layer.

#### 3.3.1 A porous layer with different porous rates

The interfacial layer is set to be an YSZ porous layer with a thickness of 1-micron and an interfacial resistance 0.3 Ω. The porous rate varies from 0% to 70%. The simulated working condition is at 800 ˚ C, the applied voltage is 1.5 volts, the gas flow rates are kept constant during the electrolysis operation as 4.5 Nl/min $H_2$ and 4.5 Nl/min $H_2O$ at fuel side and 16 Nl/min air which would affect Nernst voltage resulting $E_N$=0.935 V. The results of the simulation are shown in Tab.3 and Fig. 3.12.

The results show that the ionic current density is about 1.6 $Acm^{-2}$ and the electronic current density is very small. The ionic current density 1.6 $Acm^{-2}$ is large enough to give a high efficiency of the cell. The oxygen partial pressure is high, much larger than oxygen partial pressure in air, meaning that certain amount of oxygen gas may accumulate closed pores/cavities of the electrolyte. The oxygen gas at closed pores/cavities at the solid-solid two-phase (oxygen electrode and electrolyte) interface could diffuse rapidly into air because of the porous layer at the cathode/electrolyte interface.

The effect of the porous rate 0-70% is not significant. In the next research, a 20% porous rate of the interfacial porous layer is used to guarantee the interfacial bond strength.

Table 3 Results for different porous rates

| Porous Rate | Electronic Current ($A\ cm^{-2}$) | Ionic Current ($A\ cm^{-2}$) | Electrolyte Resistance (ASR) ($\Omega\ cm^2$) | Oxygen partial pressure (atm) |
|---|---|---|---|---|
| 0% (dense layer) | 0.024 | 1.642 | 62.257 | $1.46\times10^6$ |
| 30% | 0.024 | 1.639 | 62.257 | $1.40\times10^6$ |
| 50% | 0.024 | 1.629 | 62.257 | $1.23\times10^6$ |
| 70% | 0.023 | 1.445 | 62.572 | $1.15\times10^6$ |

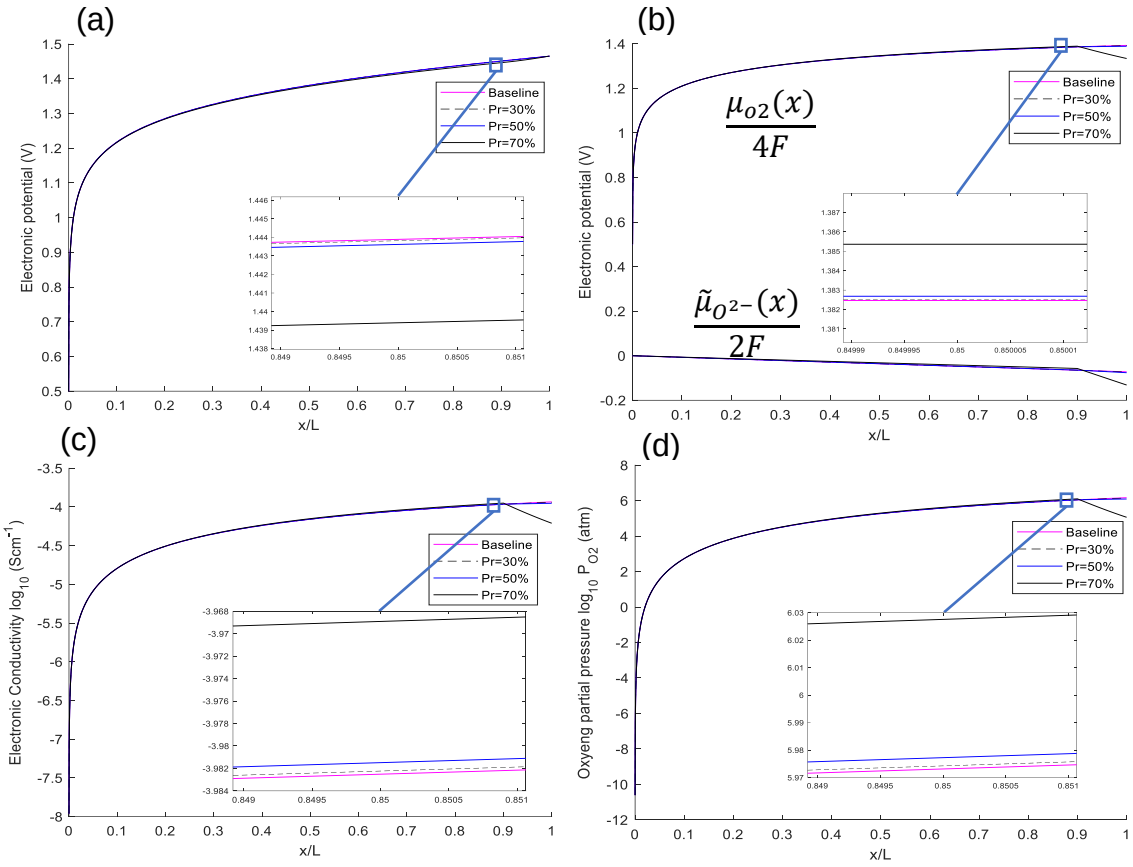


Figure 3.12 Simulation results for cells with an interfacial porous layer of different porous rates. (a) $\varphi$(x) in the electrolyte. (b) $\frac{\tilde{\mu}_{O^{2-}}(x)}{2F}$ and $\frac{\mu_{o2}(x)}{4F}$ as a function of distance in the electrolyte. (c) Electronic conductivity as a function of oxygen partial pressure. (d) Oxygen partial pressure as a function of distance in the electrolyte.

### 3.3.2 A porous layer with different thicknesses

The interfacial layer is set to be an YSZ porous layer with a porous rate 20% and an interfacial resistance 0.3 Ω. The thickness of the porous layer varies thickness of YSZ porous layer varies from 0 to 4 microns, and the dense layer of the electrolyte stays 10 microns. The simulated working condition is at 800 ˚ C, the applied voltage is 1.5 volts, the gas flow rates are kept constant during the electrolysis operation as 4.5 Nl/min $H_2$ and 4.5 Nl/min $H_2O$ at fuel side and 16 Nl/min air which would affect Nernst voltage resulting $E_N$=0.935 V. The results of the simulation are shown in Tab.4 and Fig. 3.13.

The results show that the ionic current density is about 1.6 $Acm^{-2}$ and the electronic current density is very small. The ionic current density 1.6 $Acm^{-2}$ is large enough to give a high efficiency of the cell. The oxygen partial pressure is high, much larger than oxygen partial pressure in air. The oxygen gas at

closed pores/cavities at the oxygen electrode and electrolyte interface could diffuse rapidly into air because of the porous layer at the cathode/electrolyte interface. The ionic current density and the oxygen partial pressure will decrease with the increase of the thickness of the interfacial porous layer.

Table 4 Results for different thicknesses of the porous layer

| Thickness (μm) | Electronic Current (A $cm^{-2}$) | Ionic Current (A $cm^{-2}$) | Electrolyte Resistance (ASR Ω $cm^2$) | Oxygen partial pressure (atm) |
|---|---|---|---|---|
| 0.0 | 0.024 | 1.642 | 62.257 | $1.46\times10^6$ |
| 0.1 | 0.024 | 1.642 | 62.257 | $1.45\times10^6$ |
| 0.5 | 0.024 | 1.641 | 62.257 | $1.43\times10^6$ |
| 2.0 | 0.024 | 1.639 | 62.262 | $1.40\times10^6$ |
| 4.0 | 0.024 | 1.419 | 62.288 | $1.36\times10^6$ |

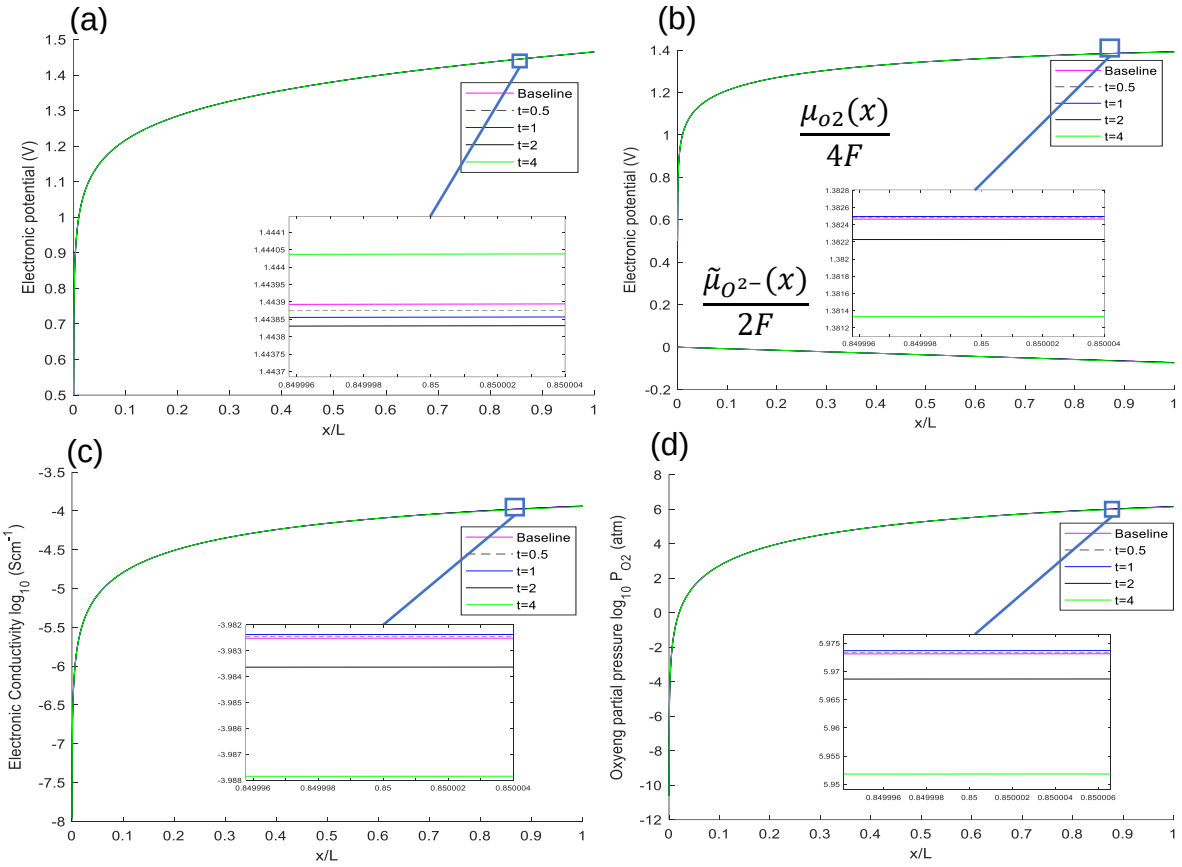


Figure 3.13 Simulation results for cells with an interfacial porous layer of different thicknesses. (a) $\varphi$(x) in the electrolyte. (b) $\frac{\tilde{\mu}_{O^{2-}}(x)}{2F}$ and $\frac{\mu_{O2}(x)}{4F}$ as a function of distance in the electrolyte. (c) Electronic conductivity as a function of oxygen partial pressure. (d) Oxygen partial pressure as a function of distance in the electrolyte.

### 3.3.3 A porous layer with different Nernst voltage

The interfacial layer is set to be an YSZ porous layer with a porous rate 20% and an interfacial resistance 0.3 Ω, with Nernst voltage varies from 0.8 to 1.1245 V. The simulated working condition is at 800 ˚ C, the applied voltage is 1.5 volts, the gas flow rates are kept constant during the electrolysis operation can be changed resulting different Nernst voltages. The results of the simulation are shown in Fig. 3.14 and Tab. 5

The results show that the ionic current density is about 1.2-2.0 $Acm^{-2}$ and the electronic current density is very small. The ionic current density is large enough to give a high efficiency of the cell. The oxygen partial pressure ranges from $7.70\times10^{5}$ atm to $3.49\times10^{6}$ atm. The oxygen partial pressure is still high, much larger than oxygen partial pressure in air. The ionic current density and the oxygen partial pressure will change significantly with Nernst voltages.

Table 5 Results for different Nernst voltages

| Nernst voltage (V) | Electronic Current (A $cm^{-2}$) | Ionic Current (A $cm^{-2}$) | Electrolyte Resistance (ASR Ω $cm^{2}$) | Oxygen partial pressure (atm) |
|---|---|---|---|---|
| 0.935 Baseline | 0.024 | 1.642 | 62.257 | $1.46\times10^{6}$ |
| 0.8 | 0.022 | 2.033 | 67.226 | $7.70\times10^{5}$ |
| 0.935 | 0.024 | 1.641 | 62.257 | $1.43\times10^{6}$ |
| 1.0645 | 0.025 | 1.265 | 57.644 | $2.66\times10^{6}$ |
| 1.1245 | 0.026 | 1.246 | 55.883 | $3.49\times10^{6}$ |

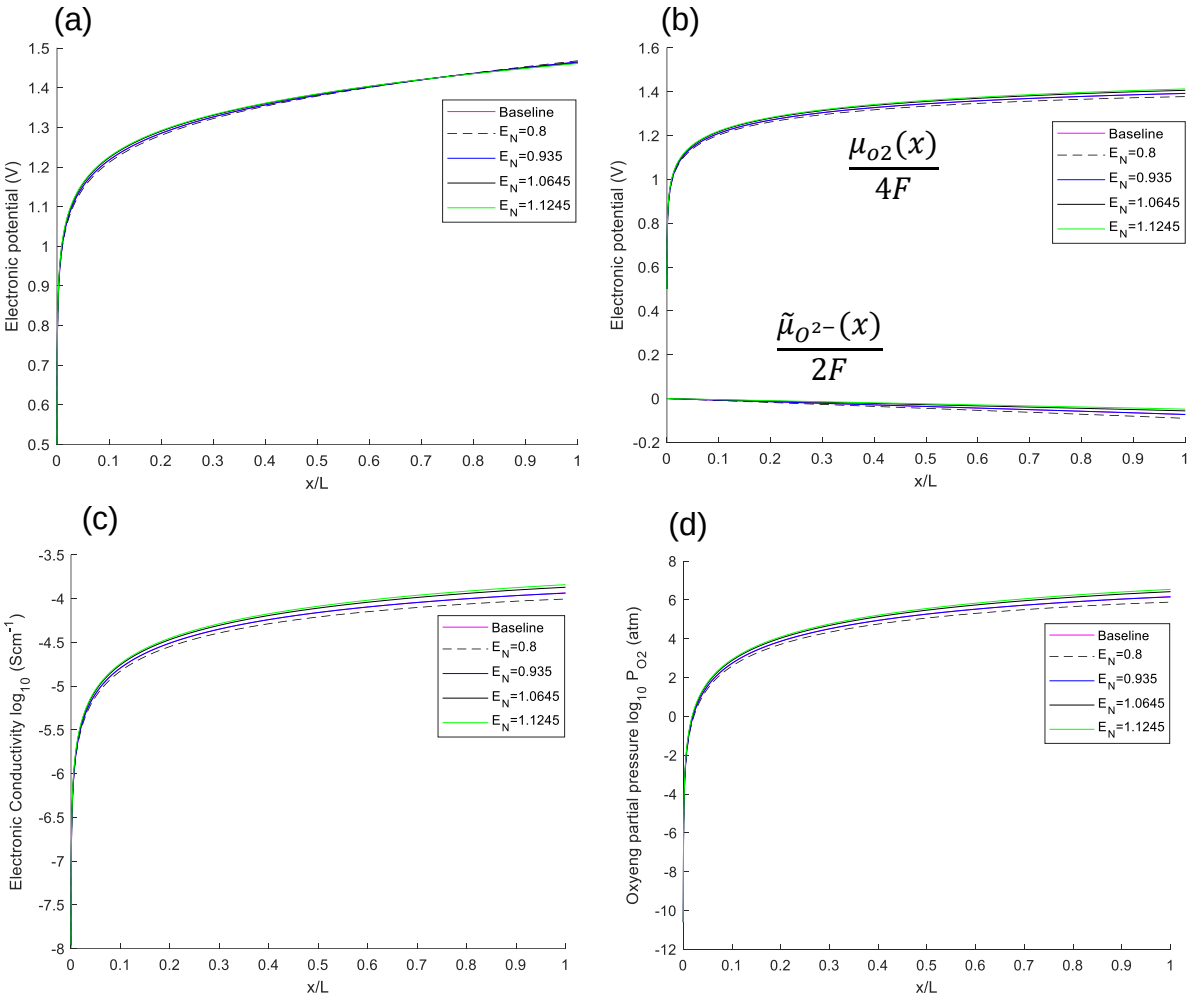


Figure 3.14 Simulation results for cells with different Nernst voltages. (a) $\varphi$(x) in the electrolyte. (b) $\frac{\tilde{\mu}_{O^{2-}}(x)}{2F}$ and $\frac{\mu_{o2}(x)}{4F}$ as a function of distance in the electrolyte. (c) Electronic conductivity as a function of oxygen partial pressure. (d) Oxygen partial pressure as a function of distance in the electrolyte.

### 3.3.4 A porous layer with different interfacial resistances

The interfacial layer is set to be an YSZ porous layer with a porous rate 20% and a thickness 1-micron. The interfacial resistance varies from 0.1 to 3 Ω. The simulated working condition is at 800 ˚ C, the applied voltage is 1.5 volts, the gas flow rates are kept constant during the electrolysis operation as 4.5 Nl/min $H_2$ and 4.5 Nl/min $H_2O$ at fuel side and 16 Nl/min air which will affect Nernst voltage resulting $E_N$=0.935 V. The results of the simulation are shown in Tab.6 and Fig. 3.15.

The results show that the ionic current density is about 1.0-3.9 $Acm^{-2}$ and the electronic current density is very small. The ionic current density is large enough to give a high efficiency to the cell. The oxygen partial pressure ranges from $3.34\times10^{4}$ atm to $3.79\times10^{6}$ atm. The oxygen partial pressure is still high, much larger than oxygen partial pressure in air. The ionic current density and the oxygen partial pressure will change significantly with the interfacial resistances. The interfacial resistance of 0.1 $\Omega cm^{2}$ is suitable for obtaining a high ionic current density 3.9 $Acm^{-2}$ and a relatively low oxygen partial pressure $3.34\times10^{4}$ atm.

Table 6 Results for different Interfacial resistances

| Interfacial resistances (ASR Ω $cm^{2}$) | Electronic Current (A $cm^{-2}$) | Ionic Current (A $cm^{-2}$) | Electrolyte Resistance (ASR Ω $cm^{2}$) | Oxygen partial pressure (atm) |
|---|---|---|---|---|
| 0.3 Baseline | 0.024 | 1.642 | 62.257 | $1.46\times10^{6}$ |
| 0.1 | 0.014 | 3.913 | 104.708 | $3.34\times10^{4}$ |
| 0.3 | 0.024 | 1.641 | 62.257 | $1.43\times10^{6}$ |
| 0.5 | 0.026 | 1.038 | 55.374 | $3.79\times10^{6}$ |
| 3.0 | 0.031 | 1.240 | 47.602 | $1.48\times10^{7}$ |

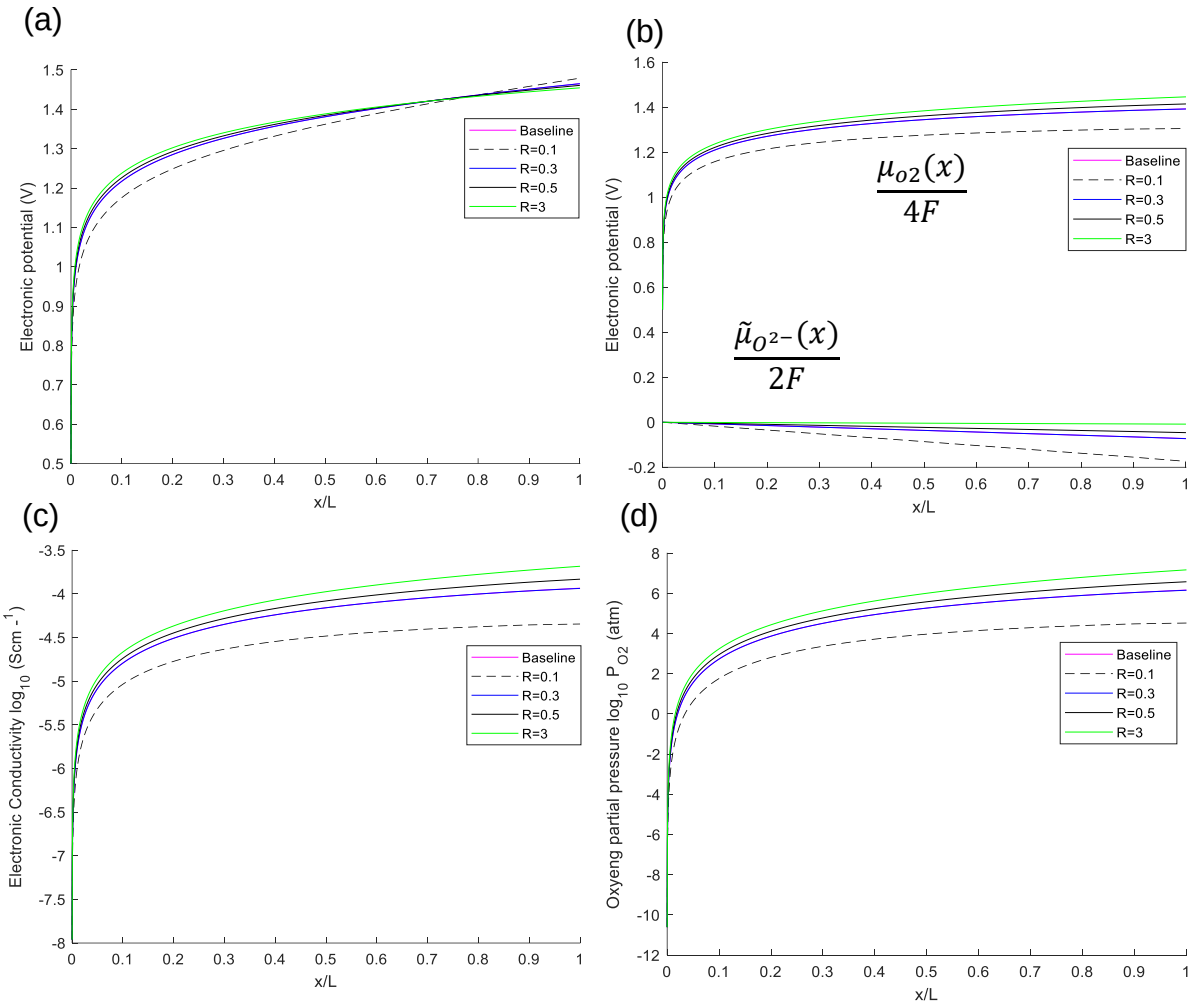


Figure 3.15 Simulation results for cells with different interfacial resistances. (a) $\varphi$(x) in the electrolyte. (b) $\frac{\tilde{\mu}_{O^{2-}}(x)}{2F}$ and $\frac{\mu_{o2}(x)}{4F}$ as a function of distance in the electrolyte. (c) Electronic conductivity as a function of oxygen partial pressure. (d) Oxygen partial pressure as a function of distance in the electrolyte.

### 3.4 Summary

(1) The experiments cannot fully explain the electrochemical mechanism of SOEC. Thus, a model of the cathode/electrolyte interfacial porous layer for electrochemical mechanism needs to be considered. The theory of thermodynamic and electrochemical equilibrium is introduced.

(2) A thermodynamic and electrochemical equilibrium model is established by considering a cathode/electrolyte interfacial porous layer. Numerical results are obtained for degenerated non-porous layer. The results show good agreement with the existing result in references. The simulation of the model is verified to guarantee its validity.

(3) In order to analyze the influence of interface microstructure parameters on cell performance, such as porous layer porosity, thickness, Nernst voltage and interfacial resistances, etc., these parameters are studied separately to find reasonable interface porous layer parameters and provide reference for the design of the interfacial layer. The results show that the ionic current density and the oxygen partial pressure will change significantly with the interfacial resistances and Nernst voltages. The porous rate and the thickness of the cathode/electrolyte interfacial layer have little impact on the cell efficiency.

(4) By using numerical experiments, the one dimensional thermodynamic and electrochemical equilibrium model with porous layer provides a guideline for designing and optimism SOECs.

## 4. Innovations of the SOFC Chromium poisoning

### 4.1 Reaction Mechinenism of Chromium poisoning (LSCF system)

- **Chromium Source**

The Cr source of the Cr poisoning is mainly coming from the interconnects of the SOFC stack as shown in Fig.4.1 [114]. Interconnects play an important role in the SOFC stacks. Electrical connection is established by the interconnects between the anode of an individual cell to the cathode of the next cell and acts as physical barrier to avoid any contact between the reducing and the oxidizing atmospheres. The criteria for the interconnect materials are the most stringent of all cell components.

The reason to choose chromium based (chromia formation) alloys is because chromia has high conductivity compared to other oxides [115,116]. However, due to its chromium content, the chromium poisoning for cathode and excessive chromia growth are inevitable.

Note that low Cr content (5% and 10%) has also been used as interconnect, but the oxidation resistance was reduced significantly when lowering the Cr content [117,118]. Low Cr steels (<5% Cr) consist of nearly pure Fe oxide accompanied by internal oxide precipitates of $Cr_2O_3$ and/or $FeCr_2O_4$ spinels. With increasing Cr content, the scales become richer in spinel and chromia, which is accompanied by a decrease of the scale growth rate.

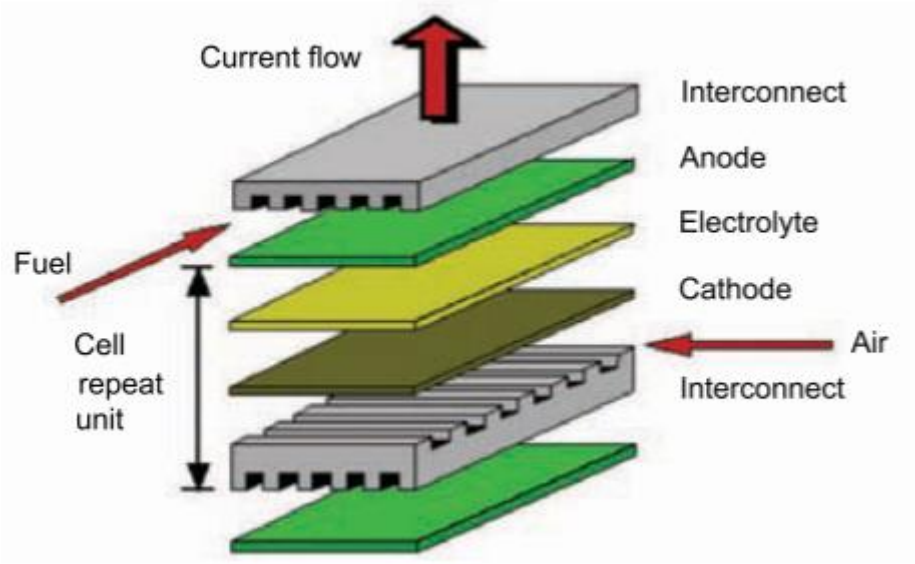


Figure 4.1 Planar design for a solid oxide fuel cell (exploded view) [114]

The alloys used as metallic interconnects form $Cr_2O_3$ under cathodic [$P(O_2)$ = $2.13\times10^4$ Pa] and anodic [$P(O_2)$ = $10^{-12}$ to $10^{-7}$ Pa] conditions [93]. ($P(O_2)$ is very small in Anodic condition, thus only consider the cathodic condition) A thin layer of this oxide grows on the surface of the alloy. The oxide completely covers the alloy surface and determines the chromium vaporization.

In the LSCF electrode, the Cr poisoning is more server compare to the LSM electrode. The experiment [119] shows that Cr poisoning of the LSCF not only has $Cr_2O_3$ redeposition, the crystallization of the Cr–Sr–O would cause the formation of $SrCrO_4$ as shown in the figure 4.2

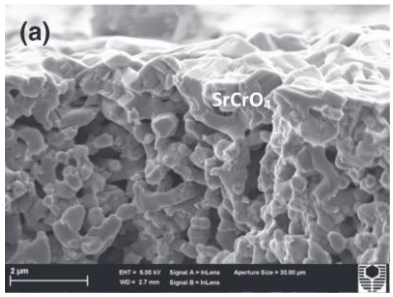


Figure 4.2 SEM of the cross-section of (a) LSCF outer surface [119]

- **Chromium vaporization (under dry air working condition)**

Chromium poisoning is caused by Chromium vapor transportation form the interconnect to the cathode under SOFC mode as shown in the Fig. 4.3 [120]. The thermodynamic instability of the chromia scales formed on the chromia-contained alloys at high temperatures, forming gaseous species through the following reactions:

$$Cr_2O_{3(s)} + xO_{2(g)} \rightarrow 2CrO_{i(g)} \quad (i = 1,2,3) \qquad (4\text{-}1)$$

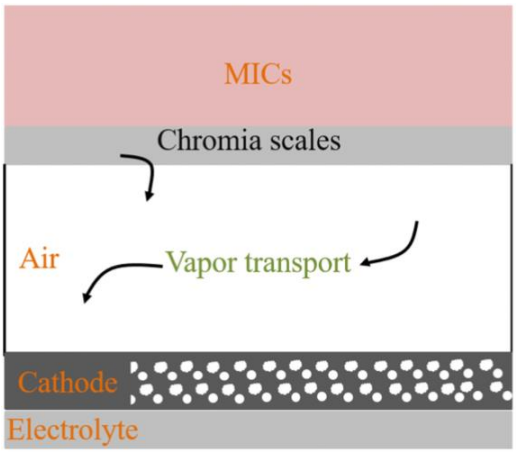


Figure 4.3 Schematic of electrochemically reduced Cr transport to cathode in SOFC [120].

The vapor pressures of chromium containing species over $Cr_2O_3$ or other chromium containing oxides have been well investigated [93,121].

The volatile Cr species from the chromia scale strongly depend on the partial pressure of oxygen. $CrO_3$(g), $CrO_2$(g), and CrO(g) have different vapor pressures over $Cr_2O_3$ as a function oxygen potential. With increasing oxygen partial pressure, equilibrium vapor pressure of such species increases.

The vapor pressure of $CrO_3$(g) exhibits large temperature dependence.

- **Chromium deposition (under dry air working condition)**

Due to the electrochemical reduction of the Cr gaseous species, $Cr_2O_3$ formed on the cathode/electrolyte interface (as illustrated in Fig. 4.3) which is predominantly based on the thermodynamic activity of the negative Gibbs energy changes [93] by:

$$2CrO_{3(g)} + 6e^- \rightarrow Cr_2O_{3(s)} + 3O^{2-} \quad (4\text{-}2)$$

where $CrO_3$ is the main Cr gaseous species.

Another study by Konysheva et al. [122] shows that Cr species distributes randomly all over the cathode for the sample tested with no current, which is attributed to the decomposition of the cathode, while Cr species deposited mainly at the TPB for the sample tested with applied current load. This preferential $Cr_2O_3$ deposition at the TPB supports the electrochemical mechanism and is reported by many researchers [93,121,122,123].

Additionally, the chromia scale itself has low electronic conductivity where interdiffusion of cation species like Cr, Co, Fe, Mn and Sr at the interconnects and oxygen electrode (or contact layer) interface will create layers with increased ohmic resistance [124].

For the LSCF electrode, chemical reaction of Cr deposition is the following reaction:

$$SrO + CrO_3 \rightarrow Cr\text{–}Sr\text{–}O_x\ (nuclei) + CrO_3 + SrO \rightarrow SrCrO_4 \quad (4\text{-}3)$$

Sr species is originally enriched or segregated at the surface of LSCF. Sr-enriched regions are in the form of SrO. The nucleation between the static SrO and gaseous Cr species occur at the first contact, leading to the formation of Sr–Cr–O nuclei and then crystallization and grain growth of SrCrO4 and Cr2O3 solid phases.

Since $SrCrO_4$ is nonconductive, the $SrCrO_4$ formation inside cathodes leads to lowering in appearance conductivity and lowering in porosity. $SrCrO_4$ can increase in the thermal expansion coefficient.

## 4.2 Methods used to mitigate Cr poisoning

Chromia-containing deposits were seen to cover the electrochemically active sites at the triple phase boundaries [92,108]. Various factors such as high operating temperatures [89,97, 125 ], the nucleation agent [90], nature of the electrode and electrolyte [89,126,127], the presence of humidity [109,128], cathodic current [95,129], cathodic polarization [89, 128], low sintering temperatures [127], and concentration of chromium [ 130 ] have been known to affect the corrosion phenomena. The following mitigation measures have been proposed:

1). Avoiding direct contact of the electrodes with the chromia-forming interconnects, by having a GDC nanoparticles buffer layer, as shown by SEM-EDS results [131,132].

2). Operating the SOFC at low temperatures, which reduced Sr segregation and decreased the partial pressure of Cr vapors [97, 133 ]. However, low temperatures were not feasible for SOFC operation with LSM cathodes [126,134].

3). Using novel electrodes such as LNF [80, 94] and NNO ($Nd_{1.95}NiO_{4+\delta}$). But these electrodes have not yet been put to practical applications [98,135].

4). Coating of the interconnect surface [136] with manganese-based spinel (e.g., $CuMn_{1.8}O_4$, $(Mn, Co)_3O_4$, and $Mn_{1.5}Co_{1.5}O_4$ coating studied by Yang et al. [83]). This suppressed the vaporization of Cr and provided high electronic conductivity. However, it led to the degradation of the structure of the interconnect and the coating process was difficult [92].

Method used to prevent Cr poisoning is Blocking Cr Vaporization: Limited availability of the oxygen to the surface of alloy and because of high free energy for oxide formation, Al is found to be only alloying element enriched in the protective film, and other alloying elements such as Cr, Fe, and Ni remain metallic as shown in Fig. 4.4 [137].

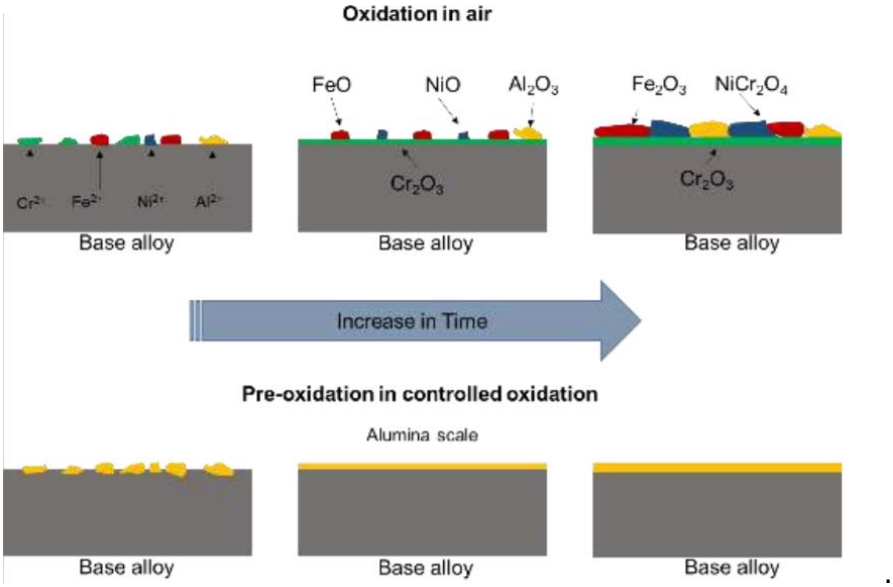


Figure 4.4 Oxidation in air with and without Al scale [137]

The Cr vaporization can be reduced by having a Ce/Co-coated stainless steel interconnector [138], Fig. 4.4 shows the Cr vaporization differences between the coated and uncoated interconnectors. The Ce/Co-coated stainless steel interconnector showed the vaporization almost kept zero over time.

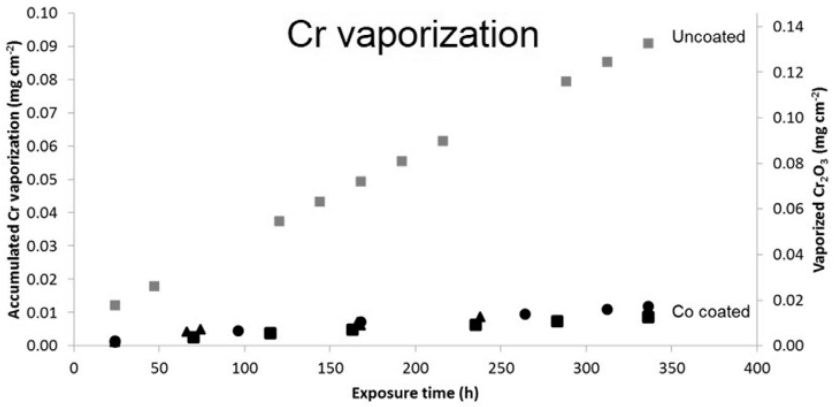


Figure 4.5 Accumulated Cr vaporization as a function of time at 850°C in air [138].

5). Modifying the interconnect alloy by adding manganese [89].

6). Reducing the measure of Cr vapors by incorporating porous and electrically conducting chromium getter layers (made of high-temperature stable compound $Sr_9Ni_7O_{21}$) on or close to the cathode. This, however, adversely affected electrical performance [83,92].

7). Coating of the cathode surface with CoNi foam (acting as a current collector). This alleviated ASR deterioration [139].

8). Impregnating with BaO led to the preferential formation of $BaCrO_4$ instead of $SrCrO_4$, thus, inhibiting the Sr segregation.

9). Inserting doped ceria counteracted Cr deposition and enhanced the volatilization of deposited Cr with catholically emitted water vapors from ceria [140].

10). Modifying the surface of the electrodes by coating with hybrid catalysts composed of a conformal film of perovskite $PrNi_{0.5}Mn_{0.5}O_3$ (PNM) with exsoluted $PrO_x$ nanoparticles as shown by Raman spectroscopy results [135].

## 4.3 Proposed new approach to improve cell performance

Form chapter 4.2 the current method of mitigation Cr poisoning is mostly focused on the coating or reduce Cr vapor with additional layers. These methods are proved to be effective, yet additional manufacturing process is needed. On the other hand, the proposed methods of mitigation Cr poisoning consider the Cr vapor forming environments i.e., the oxygen partial pressure and working temperature. As mentioned in chapter 4.1, the volatile Cr species from the chromia scale strongly depend on the partial pressure of oxygen.

The proposed method meant to avoid Cr poisoning can be by controlling the partial pressure of oxygen where $CrO_3$ will not become the dominating gaseous species.

## 4.4 Theorical support

### 4.4.1 Thermodynamic stability for Cr-O system

The Cr-O system phase diagram Fig. 4.6 shows the thermodynamic stability of different phases vs P($O_2$), Dominating Cr-based gas pressures are different in regions I, II, and III . In region I, the dominating gaseous species is Cr gas; In region II, the dominating gaseous species is $CrO_2$ (colored in blue line reaction in Tab.4.1 (10)); In region III, the dominating gaseous species is $CrO_3$ (colored in purple line reaction in Tab.4.1 (13)). The reaction equations are shown in Tab 4.1.

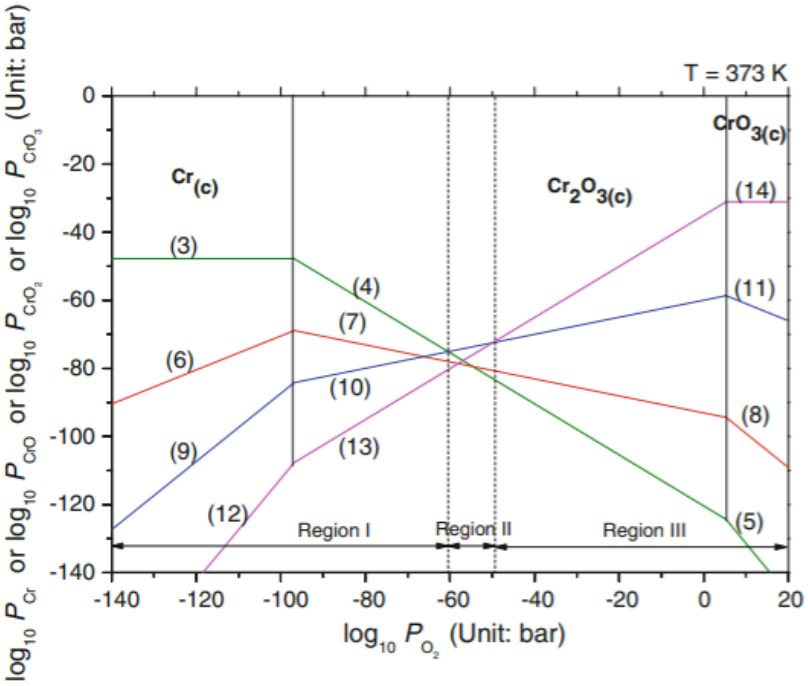


Figure 4.6 Volatility diagram for Cr-O system at 373 K [141]

By controlling the $PO_2$ during the SOFC operation to stay in region II where reaction Tab.4.1 (10) has higher partial pressure that reaction Tab.4.1 (13). $CrO_3$ becomes the dominating gaseous species can be avoided.

The experimental SOFC operation condition is usually about 750 ˚C. In Fig. 4.6 the Volatility diagram for Cr-O system temperature is 373 K, it is below the desired SOFC experimental temperature 1023 K. Thus, a new volatility diagram for Cr-O system at 1023 K is needed to determine the ideal oxygen partial pressure that $CrO_3$ is not the dominating gaseous species.

### 4.4.2 Find the ideal maximum oxygen partial pressure for $CrO_3$ not becoming the dominating gaseous species

The relevant reactions for constructing the volatility diagram for the Cr-O system are given in Tab. 4.1.

The Cr vaporization reactions in SOFC operation relate to CrO, $CrO_2$ and $CrO_3$. Thus, only reaction 7, 10, and 13 is used from the table.

From the literature experiments results the relation of $CrO_3$ partial pressure and $O_2$ partial pressure is given as:

$$Cr_2O_{3(c)} + \frac{3}{2}\ O_{2(g)} = 2CrO_{3(g)} \tag{4-4}$$

For which

$$K = (P_{CrO_3})^2/(P_{O_2})^{3/2} \tag{4-5}$$

where can take from the table log K = −70.077 at 100 °C.

Table 4.1 Reactions Utilized in the Cr-O System [141]

| | | $\log_{10}(K) = -\Delta G/(2.303RT)$ | | | | |
|---|---|---|---|---|---|---|
| No. | Reaction | 373 K (100 °C) | 473 K (200 °C) | 573 K (300 °C) | 673 K (400 °C) | 773 K (500 °C) |
| 7 | $Cr_2O_3$ (c) = 2CrO (g) + 1/2 $O_2$ (g) | −186.186 | −141.439 | −112.375 | −91.991 | −78.490 |
| 10 | $Cr_2O_3$ (c) + 1/2 $O_2$ (g) = 2$CrO_2$ (g) | −119.967 | −90.831 | −71.928 | −58.685 | −49.990 |
| 13 | $Cr_2O_3$ (c) + 3/2 $O_2$ (g) = 2$CrO_3$ (g) | −70.077 | −53.814 | −43.277 | −35.902 | −30.853 |

The relation of $CrO_2$ partial pressure and $O_2$ partial pressure is obtained from the same concept:

$$Cr_2O_{3(c)} + \frac{1}{2}\ O_{2(g)} = 2CrO_{2(g)} \tag{4-6}$$

For which

$$K = (P_{CrO_2})^2/(P_{O_2})^{1/2} \tag{4-7}$$

where can take from the table log K = −119.967 at 100 °C.

From above, the ideal oxygen partial pressure for $CrO_3$ not becoming the dominating gaseous species at 100 °C is calculated as shown in the plot.

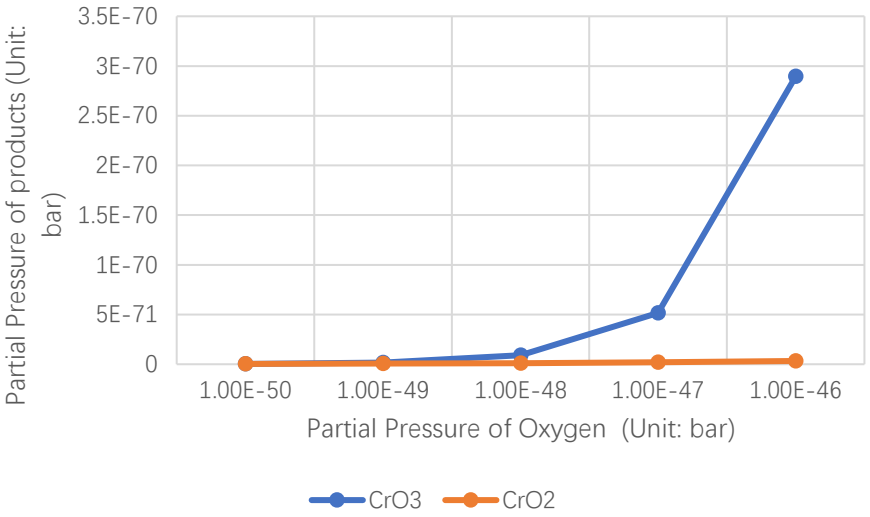


Figure 4.7 Volatility diagram for $CrO_3$ and $CrO_2$ at 373 K

The plot shows that when oxygen partial pressure is higher than $10^{-49}$ bar, $CrO_3$ become the dominating gaseous species. Fig.4.6 and Fig.4.7 shows good agreement. Following the same procedure, the volatility diagram for $CrO_3$ and $CrO_2$ at 1023 K can be calculated.

Since the log K value at 1023 K is not giving in the table, and due to the limitations. Curve fitting is used to calculate the value of log K value at 1023 K as shown in the table below.

Table 4.2 Reactions Utilized in the Cr-O System (Predicted)

| | $\log_{10}(K) = -\Delta G/(2.303RT)$ | | | | | Predicted |
|---|---|---|---|---|---|---|
| Reaction | 373 K (100 °C) | 473 K (200 °C) | 573 K (300 °C) | 673 K (400 °C) | 773 K (500 °C) | **1023 K (750 °C)** |
| $Cr_2O_3$ (c) + 1/2 $O_2$ (g) = $2CrO_2$ (g) | −119.967 | −90.831 | −71.928 | −58.685 | −78.490 | -19.346 |
| $Cr_2O_3$ (c) + 3/2 $O_2$ (g) = $2CrO_3$ (g) | −70.077 | −53.814 | −43.277 | −35.902 | −49.990 | -11.147 |

The new volatility diagram for $CrO_3$ and $CrO_2$ at 1023 K is calculated in Fig.4.8. The ideal maximum oxygen partial pressure for $CrO_3$ not becoming the dominating gaseous species is about $6.324\times10^{-9}$ bar.

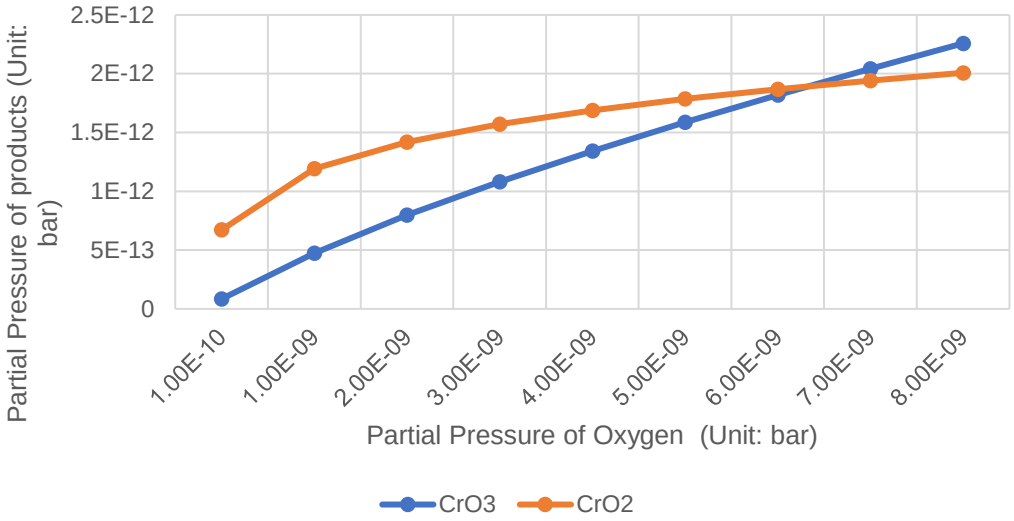


Figure 4.8 Volatility diagram for $CrO_3$ and $CrO_2$ at 1023 K

This theorical results suggested that to achieve the local oxygen partial pressure of $6.324\times10^{-9}$ bar at the TPB would help the mitigation of the Cr poisoning of the LSCF electrode. Such local oxygen partial pressure might be maintained through various way; Different current loading, adding porous layer or surface modifications.

This theorical results could also provide a possible explanation for the surface modifications of the LSCF. The Pei's experiment shows a good results [142] yet the mechanism is not clearly shown. The alleviation of Cr poisoning by surface modifications could be explain by the additional doping would increase the TPB reaction sites leading lowing the local oxygen partial pressure. Thus, limiting the formation of the $SrCrO_4$

## 4.5 Summary

(1) The Chromium poisoning mechanism is thoroughly discussed from the Cr source to the deposition and the effect of the Cr poisoning. Effect of Cr poisoning on the cathode performance. The current Cr poisoning mitigating methods are listed along with few detailed examples.

(2) The ideal maximum oxygen partial pressure for $CrO_3$ not becoming the dominating gaseous species is found to be $6.324\times10^{-9}$ bar. More specifically, the oxygen partial pressure at the TPB should not exceed this value, due to TPB is the location where most of the reaction is occurring.

(3) One way to achieve such a low oxygen partial pressure at TPB is to increase the TPB length. There are several methods to increase TPB length, first method is adding the porous YSZ layer between the electrolyte and the electrode as mentioned in chapter 3.

(4) The theorical results could provide a possible explanation of the surface modifications for Cr poisoning mitigation.

## 5. Conclusions

This thesis work is mainly focused on SOFC and SEOC theorical investigations. For SOEC investigations, a thermodynamic and electrochemical equilibrium model is established for SOECs by considering a cathode/electrolyte interfacial porous layer. Numerical results are obtained for degenerated non-porous layer. The results show good agreement with the existing result in references. The simulation of the model is verified to guarantee its validity. By using numerical experiments, the one dimensional thermodynamic and electrochemical equilibrium model with porous layer provides a guideline for designing and optimism SOECs. In order to analyze the influence of interface microstructure parameters on the performance of SOECs, such as porous layer porosity, thickness, Nernst voltage and interfacial resistances, etc., these parameters are studied separately to find reasonable interface porous layer parameters and provide reference for the design of the interfacial layer. The results show that the ionic current density and the oxygen partial pressure will change significantly with the interfacial resistances and Nernst voltages. The porous rate and the thickness of the cathode/electrolyte interfacial layer have little impact on the cell efficiency.

For SOFC investigations, the ideal maximum oxygen partial pressure for $CrO_3$ not becoming the dominating gaseous species is found to be $6.324\times10^{-9}$ bar for SOFCs. More specifically, the oxygen partial pressure at the TPB should not exceed this value, due to TPB is the location where most of the reaction is occurring. One way to achieve such a low oxygen partial pressure at TPB is to increase the TPB length. There are several methods to increase TPB length, first method is adding the porous YSZ layer between the electrolyte and the electrode. The Chromium poisoning mechanism for SOFCs is thoroughly discussed from the Cr source to the deposition and the effect of the Cr poisoning on the cathode performance. The theorical results could provide a possible explanation of the surface modifications for Cr poisoning mitigation.

**Acknowledgements**

The author would like to thank West Virginia University, Benjamin M. Statler College of Engineering and Mineral Resources and the department of mechanical and aerospace engineering; especially Prof. Xueyan Song, Prof. Ever J. Barbero and Prof. Yun Chen for discussions and advice.

## References

[1] Laguna-Bercero, M. A. "Recent advances in high temperature electrolysis using solid oxide fuel cells: A review." *Journal of Power sources* 203 (2012): 4-16.

[2] Liu, Mingyi, Bo Yu, and Jingming Xu. "Efficiency of solid oxide water electrolysis system for hydrogen production." *Journal of Tsinghua University (Science and Technology)* 6 (2009): 868.

[3] Xia, Chen, et al. "Natural mineral-based solid oxide fuel cell with heterogeneous nanocomposite derived from hematite and rare-earth minerals." *ACS Applied Materials & Interfaces* 8.32 (2016): 20748-20755.

[4] Dao, Van-Duong, et al. "Recent advances and challenges for water evaporation-induced electricity toward applications." *Nano Energy* 85 (2021): 105979.

[5] Office of Fossil Energy and Carbon Management, Why SOFC Technology? https://www.energy.gov/fecm/why-sofc-technology (2022)

[6] National energy technology laboratory, SOFC Operating principle https://netl.doe.gov/carbon-management/sofc/operating-principle

[7] He, Weidong, et al. "Gas transport in porous electrodes of solid oxide fuel cells: a review on diffusion and diffusivity measurement." *Journal of Power Sources* 237 (2013): 64-73.

[8] Stambouli, A. Boudghene, and Enrico Traversa. "Solid oxide fuel cells (SOFCs): a review of an environmentally clean and efficient source of energy." *Renewable and sustainable energy reviews* 6.5 (2002): 433-455.

[9] Bogolowski, Nicky, et al. "Activity of La0.75Sr0.25Cr0.5Mn0.5O3−δ, Ni3Sn2 and Gd-doped CeO2 towards the reverse water-gas shift reaction and carburisation for a high-temperature H2O/CO2 co-electrolysis." *RSC advances* 10.17 (2020): 10285-10296.

[10] J. Peng, el al. "Generalized Spatial-temporal Fault Location Method for Solid Oxide Fuel Cells Using LSTM and Causal Inference," in IEEE Transactions on Transportation Electrification, 2022, doi: 10.1109/TTE.2022.3187870.

[11] Guo, Haibing, et al. "Parameter extraction of the SOFC mathematical model based on fractional order version of dragonfly algorithm." International Journal of Hydrogen Energy (2022).
[12] Filonova, E., and E. Medvedev. "Recent Progress in the Design, Characterisation and Application of LaAlO3-and LaGaO3-Based Solid Oxide Fuel Cell Electrolytes. Nanomaterials 2022, 12, 1991." (2022).

[13] Stevenson, J. W., et al. "Processing and Electrical Properties of Alkaline Earth-Doped Lanthanum Gallate." Journal of the Electrochemical Society 144.10 (1997): 3613.

[14] Kumar, M., et al. "Synthesis and characterization of La0. 9Sr0. 1Ga0. 8Mg0. 2O3-δ electrolyte for intermediate temperature solid oxide fuel cells (ITSOFC)." Ionics 10.1 (2004): 93-98.

[15] Laguna-Bercero, M. A., et al. "Electrolyte degradation in anode supported microtubular yttria stabilized zirconia-based solid oxide steam electrolysis cells at high voltages of operation." *Journal of Power Sources* 196.21 (2011): 8942-8947.

[16] Chen, Kongfa. "Failure mechanism of (La,Sr) MnO3 oxygen electrodes of solid oxide electrolysis cells." *International Journal of Hydrogen Energy* 36.17 (2011): 10541-10549.

[17] Keane, Michael, et al. "LSM–YSZ interactions and anode delamination in solid oxide electrolysis cells." *international journal of hydrogen energy* 37.22 (2012): 16776-16785.

[18] Kim-Lohsoontorn, Pattaraporn, and Joongmyeon Bae. "Electrochemical performance of solid oxide electrolysis cell electrodes under high-temperature coelectrolysis of steam and carbon dioxide." *Journal of Power Sources* 196.17 (2011): 7161-7168.

[19] Hjalmarsson, Per, et al. "Influence of the oxygen electrode and inter-diffusion barrier on the degradation of solid oxide electrolysis cells." *Journal of power sources* 223 (2013): 349-357.

[20] Zhang, Shaowei, et al. "Perovskite Oxyfluoride Ceramic with In Situ Exsolved Ni–Fe Nanoparticles for Direct CO2 Electrolysis in Solid Oxide Electrolysis Cells." ACS Applied Materials & Interfaces (2022).

[21] Cao, Junwen, et al. "A Novel Solid Oxide Electrolysis Cell with Micro-/Nano Channel Anode for Electrolysis at Ultra-High Current Density over 5 A cm− 2." Advanced Energy Materials (2022): 2200899

[22] Tan, Kai, et al. "Solid oxide cells with cermet of silver and gadolinium-doped-ceria symmetrical electrodes for high-performance power generation and water electrolysis." International Journal of Hydrogen Energy (2022).

[23] Lay-Grindler, et al “Degradation Study of the La0.6Sr0.4Co0.2Fe0.8O3 Solid Oxide Electrolysis Cell (SOEC) Anode after High Temperature Electrolysis Operation. ECS Transactions, 57(1), 3177–3187. doi:10.1149/05701.3177ecst ,(2013).

[24] Zhang, Wenqiang, Bo Yu, and Jingming Xu. "Investigation of single SOEC with BSCF anode and SDC barrier layer." International journal of hydrogen energy 37.1 (2012): 837-842

[25] Energy department, www.energy.gov/fecm/science-innovation/clean-coal-research/solid-oxide-fuel-cells(2022)

[26] Tang, Eric, et al. Solid Oxide Based Electrolysis and Stack Technology with Ultra-High Electrolysis Current Density (> 3A/cm2) and Efficiency. No. DOE-FCE-0006961. FuelCell Energy, Danbury, CT (United States), 2018.

[27] Kim, Sun Jae, and Gyeong Man Choi. "Stability of LSCF electrode with GDC interlayer in YSZ-based solid oxide electrolysis cell." *Solid State Ionics* 262 (2014): 303-306.

[28] Stoots, Carl M., et al. "High-temperature electrolysis for large-scale hydrogen production from nuclear energy–experimental investigations." *International Journal of Hydrogen Energy* 35.10 (2010): 4861-4870.

[29] Virkar, Anil V. "Mechanism of oxygen electrode delamination in solid oxide electrolyzer cells." *International Journal of Hydrogen Energy* 35.18 (2010): 9527-9543.

[30] Mawdsley, Jennifer R., et al. "Post-test evaluation of oxygen electrodes from solid oxide electrolysis stacks." *international journal of hydrogen energy* 34.9 (2009): 4198-4207.

[31] Virkar, Anil V., Hyung-Tae Lim, and Greg Tao. "Failure of solid oxide fuel cells by electrochemically induced pressure." *Procedia IUTAM* 10 (2014): 328-337.

[32] Trini, Martina, et al. "Comparison of microstructural evolution of fuel electrodes in solid oxide fuel cells and electrolysis cells." *Journal of Power Sources* 450 (2020): 227599.

[33] Virkar, Anil V. "Theoretical analysis of the role of interfaces in transport through oxygen ion and electron conducting membranes." *Journal of Power Sources* 147.1-2 (2005): 8-31.

[34] Nerat, Marko, and Đani Juričić. "Modelling of anode delamination in solid oxide electrolysis cell and analysis of its effects on electrochemical performance." *International Journal of Hydrogen Energy* 43.17 (2018): 8179-8189.

[35] Su, Chaoxiang, et al. "Effects of a YSZ porous layer between electrolyte and oxygen electrode in solid oxide electrolysis cells on the electrochemical performance and stability." *International Journal of Hydrogen Energy* 44.29 (2019): 14493-14499.

[36] Park, Beom-Kyeong, et al. "Conditions for stable operation of solid oxide electrolysis cells: oxygen electrode effects." *Energy & Environmental Science* 12.10 (2019): 3053-3062.

[37] The, D., et al. "Microstructural comparison of solid oxide electrolyser cells operated for 6100 h and 9000 h." *Journal of power sources* 275 (2015): 901-911.

[38] Mogensen, Mogens Bjerg, et al. "Relation between Ni particle shape change and Ni migration in Ni–YSZ electrodes–a hypothesis." *Fuel cells* 17.4 (2017): 434-441.

[39] Jiao, Zhenjun, and Naoki Shikazono. "Study on the effects of polarization on local morphological change of nickel at active three-phase-boundary using patterned nickel-film electrode in solid oxide fuel cell anode." *Acta Materialia* 135 (2017): 124-131.

[40] Wang, W., and S. P. Jiang. "Effect of polarization on the electrode behavior and microstructure of (La,Sr) MnO3 electrodes of solid oxide fuel cells." *Journal of Solid State Electrochemistry* 8.11 (2004): 914-922.

[41] Backhaus-Ricoult, M., et al. "In-situ study of operating SOFC LSM/YSZ cathodes under polarization by photoelectron microscopy." *Solid State Ionics* 179.21-26 (2008): 891-895.

[42] Chen, Kongfa, and Na Ai. "Reasons for the high stability of nano-structured (La,Sr)MnO3 infiltrated Y2O3–ZrO2 composite oxygen electrodes of solid oxide electrolysis cells." *Electrochemistry communications* 19 (2012): 119-122.

[43] Rashkeev, Sergey N., and Michael V. Glazoff. "Atomic-scale mechanisms of oxygen electrode delamination in solid oxide electrolyzer cells." *international journal of hydrogen energy* 37.2 (2012): 1280-1291.

[44] Sreedhar, I., et al. "Recent advances in material and performance aspects of solid oxide fuel cells." *Journal of Electroanalytical Chemistry* 848 (2019): 113315.

[45] Sreedhar, I., et al. "An overview of degradation in solid oxide fuel cells-potential clean power sources." *Journal of Solid State Electrochemistry* 24.6 (2020): 1239-1270.

[46] Yokokawa, Harumi, et al. "Fundamental mechanisms limiting solid oxide fuel cell durability." *Journal of Power Sources* 182.2 (2008): 400-412.

[47] Vassen, R., D. Simwonis, and D. Stöver. "Modelling of the agglomeration of Ni-particles in anodes of solid oxide fuel cells." *Journal of materials science* 36.1 (2001): 147-151.

[48] Holzer, Lorenz, et al. "Microstructure degradation of cermet anodes for solid oxide fuel cells: Quantification of nickel grain growth in dry and in humid atmospheres." *Journal of Power Sources* 196.3 (2011): 1279-1294.

[49] Ioselevich, A., A. A. Kornyshev, and W. Lehnert. "Degradation of solid oxide fuel cell anodes due to sintering of metal particles: correlated percolation model." *Journal of the Electrochemical Society* 144.9 (1997): 3010.

[50] Ioselevich, A., A. A. Kornyshev, and W. Lehnert. "Statistical geometry of reaction space in porous cermet anodes based on ion-conducting electrolytes: Patterns of degradation." *Solid State Ionics* 124.3-4 (1999): 221-237.

[ 51 ]Mogensen, Mogens, et al. "Progress in understanding SOFC electrodes." *Solid State Ionics* 150.1-2 (2002): 123-129.

[ 52 ] Jensen, Karin Vels, et al. "Effect of impurities on structural and electrochemical properties of the Ni–YSZ interface." *Solid State Ionics* 160.1-2 (2003): 27-37

[53] Sfeir, Joseph. *Alternative anode materials for methane oxidation in solid oxide fuel cells*. Diss. Verlag nicht ermittelbar, 2002.

[54] Matsuzaki, Yoshio, and Isamu Yasuda. "The poisoning effect of sulfur-containing impurity gas on a SOFC anode: Part I. Dependence on temperature, time, and impurity concentration." *Solid State Ionics* 132.3-4 (2000): 261-269.

[55] Gong, Mingyang, et al. "Sulfur-tolerant anode materials for solid oxide fuel cell application." *Journal of Power Sources* 168.2 (2007): 289-298.

[ 56 ] Evans, A. G. "Considerations of inhomogeneity effects in sintering." Journal of the American ceramic Society 65.10 (1982): 497-501.

[ 57 ] Fischer, W., et al. "Residual stresses in planar solid oxide fuel cells." *Journal of Power Sources* 150 (2005): 73-77.

[ 58 ] Wakui, T., J. Malzbender, and R. W. Steinbrech. "Strain dependent stiffness of plasma sprayed thermal barrier coatings." *Surface and coatings technology* 200.16-17 (2006): 4995-5002.

[59] Iwata, Tomoo. "Characterization of ni-ysz anode degradation for substrate-type solid oxide fuel cells." *Journal of the Electrochemical Society* 143.5 (1996): 1521.

[60] Simwonis, D., F. Tietz, and D. Stöver. "Nickel coarsening in annealed Ni/8YSZ anode substrates for solid oxide fuel cells." *Solid State Ionics* 132.3-4 (2000): 241-251.

[61] Hagen, Anke, et al. "Degradation of anode supported SOFCs as a function of temperature and current load." *Journal of the Electrochemical Society* 153.6 (2006): A1165.

[62] Khan, Muhammad Shirjeel, et al. "Fundamental mechanisms involved in the degradation of nickel–yttria stabilized zirconia (Ni–YSZ) anode during solid oxide fuel cells operation: a review." *Ceramics International* 42.1 (2016): 35-48.

[63] Sasaki, K., et al. "H2S poisoning of solid oxide fuel cells." *Journal of the Electrochemical Society* 153.11 (2006): A2023.

[64] Zha, Shaowu, Zhe Cheng, and Meilin Liu. "Sulfur poisoning and regeneration of Ni-based anodes in solid oxide fuel cells." *Journal of the Electrochemical Society* 154.2 (2006): B201.

[65] Yang, Lei, et al. "New insights into sulfur poisoning behavior of Ni-YSZ anode from long-term operation of anode-supported SOFCs." *Energy & Environmental Science* 3.11 (2010): 1804-1809.

[66] Li, Ting Shuai, et al. "Hydrogen sulfide poisoning in solid oxide fuel cells under accelerated testing conditions." *Journal of Power Sources* 195.20 (2010): 7025-7032.

[67] Li, Ting Shuai, and Wei Guo Wang. "The mechanism of H2S poisoning Ni/YSZ electrode studied by impedance spectroscopy." *Electrochemical and Solid-State Letters* 14.3 (2010): B35.

[68] Kromp, Alexander, et al. "Electrochemical analysis of sulphur-poisoning in anode-supported SOFCs under reformate operation." *ECS Transactions* 41.33 (2012): 161.

[69] Bartholomew, Calvin H. "Carbon deposition in steam reforming and methanation." *Catalysis Reviews Science and Engineering* 24.1 (1982): 67-112.

[70] Bartholomew, Calvin H. "Mechanisms of catalyst deactivation." *Applied Catalysis A: General* 212.1-2 (2001): 17-60.

[71] Kock, A. J. H. M., et al. "The formation of filamentous carbon on iron and nickel catalysts: II. Mechanism." *Journal of Catalysis* 96.2 (1985): 468-480.

[72] Holstein, William L. "The roles of ordinary and soret diffusion in the metal-catalyzed formation of filamentous carbon." *Journal of catalysis* 152.1 (1995): 42-51.

[73] He, Hongpeng, and Josephine M. Hill. "Carbon deposition on Ni/YSZ composites exposed to humidified methane." *Applied Catalysis A: General* 317.2 (2007): 284-292.

[74] Prakash, B. Shri, S. Senthil Kumar, and S. T. Aruna. "Properties and development of Ni/YSZ as an anode material in solid oxide fuel cell: A review." *Renewable and Sustainable Energy Reviews* 36 (2014): 149-179.

[75] Yang, Zhibin, et al. "A short review of cathode poisoning and corrosion in solid oxide fuel cell." *international journal of hydrogen energy* 42.39 (2017): 24948-24959.

[76] Hu, Boxun, et al. "Effect of CO2 on the stability of strontium doped lanthanum manganite cathode." *Journal of Power Sources* 268 (2014): 404-413.

[ 77 ] Zhao, Zhe, et al. "High-and low-temperature behaviors of La0.6Sr0.4Co0.2Fe0.8O3-δ cathode operating under CO2/H2O-containing atmosphere." *International journal of hydrogen energy* 38.35 (2013): 15361-15370.

[78] Darvish, Shadi, et al. "Thermodynamic prediction of the effect of CO2 to the stability of (La0.8Sr0.2)0.98MnO3±δ system." *International Journal of Hydrogen Energy* 41.24 (2016): 10239-10248.

[79] Wang, Zhenhua, et al. "Improved SOFC performance with continuously graded anode functional layer." *Electrochemistry Communications* 11.6 (2009): 1120-1123.

[80] Talebi, Tahereh, et al. "Investigation on microstructures of NiO–YSZ composite and Ni–YSZ cermet for SOFCs." *International Journal of Hydrogen Energy* 35.17 (2010): 9440-9447.

[81] Hashigami, Satoshi, et al. "Improvement of the redox durability of Ni-gadolinia doped ceria anodes due to the use of the composite particles prepared by spray pyrolysis method." *Journal of Power Sources* 248 (2014): 190-195.

[82] Bi, Lei, Emiliana Fabbri, and Enrico Traversa. "Effect of anode functional layer on the performance of proton-conducting solid oxide fuel cells (SOFCs)." *Electrochemistry communications* 16.1 (2012): 37-40

[83] Reisert, Michael, Ashish Aphale, and Prabhakar Singh. "Solid oxide electrochemical systems: Material degradation processes and novel mitigation approaches." *Materials* 11.11 (2018): 2169.

[84] Bucher, Edith, et al. "Sulphur poisoning of the SOFC cathode material La0.6Sr0.4Co0.2O3-δ." *Solid State Ionics* 238 (2013): 15-23.

[85] Wang, Cheng Cheng, et al. "Effect of SO2 poisoning on the electrochemical activity of La0.6Sr0.4Co0.2Fe0.8O3-δ cathodes of solid oxide fuel cells." *Journal of The Electrochemical Society* 164.6 (2017): F514.

[86] Wang, Fangfang, et al. "The correlation of sulfur distribution in LSCF and performance degradation under different operation temperatures." *ECS Transactions* 78.1 (2017): 927.

[87] Wang, Cheng Cheng, and Kongfa Chen. "Sulfur deposition and poisoning of La0.6Sr0.4Co0.2Fe0.8O3-δ cathode materials of solid oxide fuel cells." *Journal of The Electrochemical Society* 161.12 (2014): F1133.

[88] Wang, Cheng Cheng, et al. "Effect of SO2 poisoning on the electrochemical activity of La0.6Sr0.4Co0.2Fe0.8O3-δ cathodes of solid oxide fuel cells." *Journal of The Electrochemical Society* 164.6 (2017): F514.

[89] Fergus, Jeffrey W. "Effect of cathode and electrolyte transport properties on chromium poisoning in solid oxide fuel cells." *International Journal of Hydrogen Energy* 32.16 (2007): 3664-3671.

[90] Jiang, San Ping, Sam Zhang, and Y. D. Zhen. "Early interaction between Fe–Cr alloy metallic interconnect and Sr-doped LaMnO3 cathodes of solid oxide fuel cells." *Journal of materials research* 20.3 (2005): 747-758.

[91] Zhen, Yongda. "Mechanism of Cr deposition and its application in the development of Cr-tolerant cathodes of solid oxide fuel cells." *Solid State Ionics* 179.27-32 (2008): 1459-1464.

[92] Liang, Chiying, et al. "Mitigation of chromium assisted degradation of LSM cathode in SOFC." *ECS Transactions* 75.28 (2017): 57.

[93] Hilpert, K., et al. "Chromium vapor species over solid oxide fuel cell interconnect materials and their potential for degradation processes." *Journal of the Electrochemical Society* 143.11 (1996): 3642.

[94] Jiang, S. P., et al. "Deposition of chromium species at Sr-doped LaMnO3 electrodes in solid oxide fuel cells. I. Mechanism and kinetics." *Journal of the Electrochemical Society* 147.11 (2000): 4013.

[95] Li, Jun, et al. "The investigation of Cr deposition and poisoning effect on Sr-doped lanthanum manganite cathode induced by cathodic polarization for intermediate temperature solid oxide fuel cell." *Electrochimica Acta* 255 (2017): 31-40.

[96] Wei, Bo, et al. "Chromium deposition and poisoning at La0.6Sr0.4Co 0.2Fe0.8O3−δ oxygen electrodes of solid oxide electrolysis cells." *Physical Chemistry Chemical Physics* 17.3 (2015): 1601-1609.

[97] Wei, Bo, et al. "Cr deposition on porous La0.6Sr0.4Co0.2Fe0.8O3−δ electrodes of solid oxide cells under open circuit condition." *Solid State Ionics* 281 (2015): 29-37.

[98] Chen, Xinbing. "Chromium deposition and poisoning of cathodes of solid oxide fuel cells–a review." *International Journal of Hydrogen Energy* 39.1 (2014): 505-531.

[99] Zhang, Sam, and Y. D. Zhen. "Deposition of Cr species at (La,Sr)(Co,Fe) O3 cathodes of solid oxide fuel cells." *Journal of The Electrochemical Society* 153.1 (2005): A127.

[100] Amezawa, Koji, et al. "Mechanism of chromium poisoning in SOFC cathode investigated by using pattern thin film model electrode." *ECS Transactions* 78.1 (2017): 965.

[101] Krishnan, Sridevi, et al. "First principles study of Cr poisoning in solid oxide fuel cell cathodes: Application to (La,Sr)CoO3." *Computational Materials Science* 137 (2017): 6-9.

[102] Chen, Xinbing, Lan Zhang, and Erjia Liu. "A fundamental study of chromium deposition and poisoning at (La0.8Sr0.2)0.95(Mn1−xCox)O3±δ (0.0≤ x≤ 1.0) cathodes of solid oxide fuel cells." *international journal of hydrogen energy* 36.1 (2011): 805-821.

[103] Horita, Teruhisa, et al. "Chromium poisoning and degradation at (La, Sr) MnO3 and (La, Sr) FeO3 cathodes for solid oxide fuel cells." *Journal of The Electrochemical Society* 157.5 (2010): B614.

[104] Stodolny, M. K., et al. "Impact of Cr-poisoning on the conductivity of LaNi0. 6Fe0.4O3." *Journal of power sources* 196.22 (2011): 9290-9298.

[105] Gross, Michael D., John M. Vohs, and Raymond J. Gorte. "A strategy for achieving high performance with SOFC ceramic anodes." *Electrochemical and solid-state letters* 10.4 (2007): B65.

[106] Chen, Kongfa, et al. "Performance of an anode-supported SOFC with anode functional layers." *Electrochimica Acta* 53.27 (2008): 7825-7830.

[107] Suzuki, Toshio, et al. "Effect of anode functional layer on energy efficiency of solid oxide fuel cells." *Electrochemistry communications* 13.9 (2011): 959-962.

[108] Iwai, Hiroshi, et al. "Numerical Study on Progress of Cr Poisoning in LSM-YSZ Cathode of a Planar Solid Oxide Fuel Cell." *ECS Transactions* 78.1 (2017): 955.

[109] Miyoshi, Kota, et al. "Chromium poisoning in (La, Sr) MnO3 cathode: Three-dimensional simulation of a solid oxide fuel cell." *Journal of Power Sources* 326 (2016): 331-340.

[110] Zhang, Lei, Liangzhu Zhu, and Anil V. Virkar. "Modeling of oxygen chemical potential distribution in solid oxide electrolyzer cells." *Journal of The Electrochemical Society* 166.16 (2019): F1275.

[111] Hebb, Malcolm H. "Electrical conductivity of silver sulfide." *The journal of chemical physics* 20.1 (1952): 185-190.

[112] Park, Jong-Hee, and Robert N. Blumenthal. "Electronic Transport in 8 Mole Percent Y2O3-ZrO2." *Journal of the Electrochemical Society* 136.10 (1989): 2867.

[113] Yan, Yulin, et al. "Performance and degradation of an SOEC stack with different cell components." Electrochimica acta 258 (2017): 1254-1261.

[114] Wu, Junwei, and Xingbo Liu. "Recent development of SOFC metallic interconnect." *Journal of materials science & technology* 26.4 (2010): 293-305.

[115] Zhu, Wei Zhong, and S. C. Deevi. "Development of interconnect materials for solid oxide fuel cells." *Materials Science and Engineering: A* 348.1-2 (2003): 227-243.

[116] Fergus, Jeffrey W. "Lanthanum chromite-based materials for solid oxide fuel cell interconnects." *Solid State Ionics* 171.1-2 (2004): 1-15.

[117] Geng, Shujiang, et al. "A low-Cr metallic interconnect for intermediate-temperature solid oxide fuel cells." *Journal of Power Sources* 172.2 (2007): 775-781.

[118] Geng, S. J., J. H. Zhu, and Z. G. Lu. "Evaluation of Haynes 242 alloy as SOFC interconnect material." *Solid State Ionics* 177.5-6 (2006): 559-568.

[119] Wei, Bo, et al. "Cr deposition on porous La0. 6Sr0. 4Co0. 2Fe0. 8O3− δ electrodes of solid oxide cells under open circuit condition." Solid State Ionics 281 (2015): 29-37.

[120] Zhou, Lingfeng, et al. "Comprehensive review of chromium deposition and poisoning of solid oxide fuel cells (SOFCs) cathode materials." *Renewable and Sustainable Energy Reviews* 134 (2020): 110320.

[121] Yokokawa, H., et al. "Thermodynamic considerations on Cr poisoning in SOFC cathodes." *Solid State Ionics* 177.35-36 (2006): 3193-3198.

[122] Konysheva, Elena, et al. "Chromium poisoning of perovskite cathodes by the ODS alloy Cr5Fe1Y2O3 and the high chromium ferritic steel Crofer22APU." *Journal of the Electrochemical Society* 153.4 (2006): A765.

[123] Wang, Ruofan, et al. "Roles of humidity and cathodic current in chromium poisoning of Sr-doped LaMnO3-based cathodes in solid oxide fuel cells." *Journal of Power Sources* 360 (2017): 87-97.

[124] Menzler, N. H., et al. "Post-test characterization of an SOFC Short-Stack after 17,000 hours of steady operation." *ECS Transactions* 35.1 (2011): 195.

[125] Wang, Cheng Cheng, Kane O'Donnell, and Li Jian. "Co-deposition and poisoning of chromium and sulfur contaminants on La0.6Sr0.4Co0.2Fe0.8O3-δ cathodes of solid oxide fuel cells." *Journal of The Electrochemical Society* 162.6 (2015): F507.

[126] Matsuzaki, Yoshio, and Isamu Yasuda. "Dependence of SOFC cathode degradation by chromium-containing alloy on compositions of electrodes and electrolytes." *Journal of The Electrochemical Society* 148.2 (2001): A126.

[127] Xiong, Chunyan, et al. "Long-term Cr poisoning effect on LSCF-GDC composite cathodes sintered at different temperatures." *Journal of The Electrochemical Society* 163.9 (2016): F1091.

[128] Wang, Ruofan, et al. "Chromium poisoning effects on performance of (La, Sr) MnO3-based cathode in anode-supported solid oxide fuel cells." *Journal of The Electrochemical Society* 164.7 (2017): F740.

[129] Wang, Ruofan, et al. "Roles of humidity and cathodic current in chromium poisoning of Sr-doped LaMnO3-based cathodes in solid oxide fuel cells." *Journal of Power Sources* 360 (2017): 87-97.

[130] Chen, Xinbing, Yongda Zhen, and Jian Li. "Chromium deposition and poisoning in dry and humidified air at (La0.8Sr0.2)0.9 MnO3+ δ cathodes of solid oxide fuel cells." *International Journal of Hydrogen Energy* 35.6 (2010): 2477-2485.

[131] Zhao, Ling, and Sudath Amarasinghe. "Enhanced chromium tolerance of La0.6Sr0.4Co0.2Fe0.8O3− δ electrode of solid oxide fuel cells by Gd0.1Ce0.9O1.95 impregnation." *Electrochemistry communications* 37 (2013): 84-87.

[132] Zhao, L., and S. Amarasinghe. "Enhanced chromium tolerance of Gd0. 1Ce0. 9O1. 95 impregnated La0.6Sr0.4Co0.2Fe0.8O3-δ electrode of solid oxide fuel cells." *ECS Transactions* 57.1 (2013): 2163.

[ 133 ] Yin, Xiaoyan, et al. "Thermodynamic perspective of Sr-related degradation issues in SOFCs." *International journal of applied ceramic technology* 15.2 (2018): 380-390.

[134] Heo, Su Jeong, et al. "Low-Temperature Chromium Poisoning of SOFC Cathode." *ECS Transactions* 78.1 (2017): 1055.

[ 135 ] Chen, Yu, et al. "An effective strategy to enhancing tolerance to contaminants poisoning of solid oxide fuel cell cathodes." *Nano Energy* 47 (2018): 474-480.

[ 136 ] Zhang, Xiaoqiang, et al. "Mechanism of chromium poisoning the conventional cathode material for solid oxide fuel cells." *Journal of Power Sources* 381 (2018): 26-29.

[137] Aphale, Ashish N., et al. "Surface pretreatment of alumina forming alloy and its implication on Cr evaporation." *ECS Transactions* 85.2 (2018): 57.

[138] Falk-Windisch, Hannes, et al. "Chromium vaporization from mechanically deformed pre-coated interconnects in Solid Oxide Fuel Cells." *Journal of Power Sources* 297 (2015): 217-223.

[139] Lee, Jong-Ho, et al. "Suppression of chromium poisoning in SOFC cathode using chromium trapping materials." *ECS Transactions* 78.1 (2017): 1035.

[140] Yokokawa, H., et al. "Chromium Poisoning of LaMnO3-Based Cathode within Generalized Approach." *Fuel Cells* 13.4 (2013): 526-535.

[141] Hsieh, Man-Ching, et al. "Volatility diagrams for the Cr-O and Cr-Cl systems: Application to removal of Cr2O3-rich passive films on stainless steel." *Metallurgical and Materials Transactions B* 43.5 (2012): 1187-1201.

[142] Pei, Kai, et al. "Enhanced Cr-tolerance of an SOFC cathode by an efficient electro-catalyst coating." Nano Energy 72 (2020): 104704.